Natural Hazards
https://doi.org/10.1007/s11069-023-05890-6

ORIGINAL PAPER

Storm surges and coastal inundation during extreme events in the Mediterranean Sea: the IANOS Medicane

Y. Androulidakis[1,2] · C. Makris[1] · Z. Mallios[3] · I. Pytharoulis[4] · V. Baltikas[1] · Y. Krestenitis[1]

Received: 26 June 2022 / Accepted: 21 February 2023

Abstract
The IANOS Medicane was one of the most severe storms that have formed in the Mediterranean Sea with Category 2 Hurricane characteristics. The storm induced a significant increase in sea-level elevation along its pathway and caused storm surges at the central Ionian Sea with consequent impacts on coastal regions of the Ionian Islands and western Greece. An integrated approach, based on hydrodynamic ocean simulations, coupled to meteorological and coastal flooding simulations, is used in combination with field and satellite observations to analyze the marine weather conditions, the storm surge characteristics, and the coastal inundation characteristics due to the impact of IANOS Medicane in September 2020. The evolution of the Medicane and the respective storm surge in the ocean have been successfully recorded by the met-ocean simulations, part of an active public-access operational forecast system. Both wind and atmospheric pressure patterns affected the storm surge variability over the Ionian Sea. The direct intrusion of the Medicane from the central Mediterranean Sea toward the Ionian Sea formed storm surges over several coastal areas, even before the storm's landfall, due to the accompanying onshore currents. Storm surges in the order of 30 cm generated extensive flooding over lowland coastal areas, as confirmed by both satellite (Normalized Difference Water Index, NDWI) and numerical (coastal inundation modeling) data. Satellite-derived and simulated estimations showed that, in specific coastal regions, the run-up of seawater extended up to 200 m inland, depending on the hydraulic connectivity between the lowland areas, which determined the inundation extents during the storm surge.

Keywords Sea level · Low-pressure systems · Tropical-like cyclones · Mediterranean Sea · Coastal inundation · Operational modeling

✉ Y. Androulidakis
iandroul@civil.auth.gr

[1] Laboratory of Maritime Engineering and Maritime Works, School of Civil Engineering, Aristotle University of Thessaloniki, Thessaloníki, Greece

[2] Laboratory of Physical and Chemical Oceanography, Department of Marine Sciences, University of the Aegean, Mitilini, Greece

[3] Laboratory of Water Resources Engineering and Management, School of Civil Engineering, Aristotle University of Thessaloniki, Thessaloníki, Greece

[4] Department of Meteorology and Climatology, School of Geology, Aristotle University of Thessaloniki, Thessaloníki, Greece

Published online: 04 March 2023

1 Introduction

The intense atmospheric deep depressions over the Mediterranean Sea (Fig. 1a) that share similar characteristics with tropical cyclones on the order of 300 km in diameter and have windless conditions in their "eyes," along with surrounding hurricane-level (counterclockwise rotation) winds (~25 m/s; up to Category 1 Hurricane on the Saffir–Simpson scale; Emanuel 2005) and a deep warm-core structure, are termed as "Medicanes" (Miglietta et al. 2013; Cavicchia et al. 2014; Cid et al. 2016; Dafis et al. 2020; Fortelli et al. 2021; Toomey et al. 2022; Flaounas et al., 2021). Tropical cyclones and Medicanes alike are formed over the sea, intensify over warm seawaters (Noyelle et al. 2019), and weaken over the land and/or cold-water masses, often causing coastal flooding and consequent damages around the Mediterranean littoral zone (Bakkensen 2017). These low-pressure systems, accompanied by significant sea-level increases along their pathways, lead to the formation of storm surges affecting the coastal zone, due to two main mechanisms: (i) the inverse barometer effect underneath the eye of the cyclone and (ii) the wind-induced accumulation

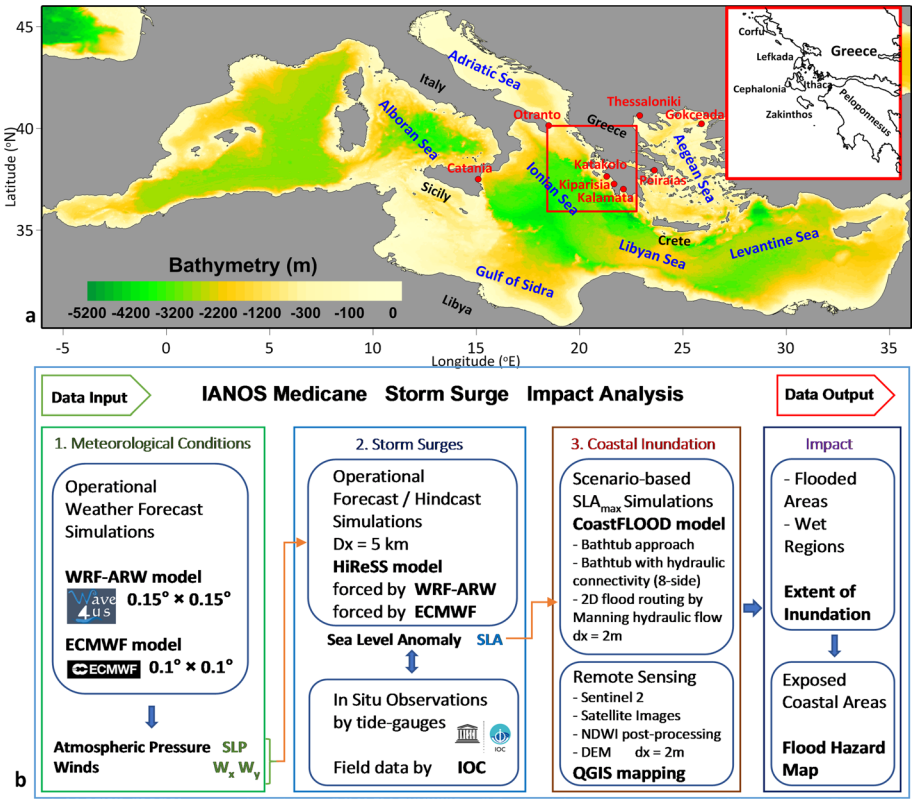

Fig. 1 **a** Bathymetry of the HiReSS model domain in the Mediterranean Sea. The names of the main topographic features, mentioned in the study, are marked. The red dots indicate the locations of the tide gauges (Intergovernmental Oceanographic Commission, IOC) that provided sea-level measurements. The inset panel shows the coastal region and the respective topographic features affected by the IANOS storm surge. **b** Flowchart of the integrated approach to analyze the impact of IANOS Medicane storm surge on the coastal zone

of seawater masses near the coast (Smith and Banke 1975). The comprehensive description of the Medicanes evolution and their impacts on the coastal zone requires integrated approaches that are capable of solving both the large-scale phenomena in the atmosphere and open sea, and the high-resolution processes (e.g., coastal flooding) in the coastal zone. Herein, we present an integrated methodology with both data-based and model-based tools, including open sea and coastal inundation modeling, plus a near-real-time forecast system (Fig. 1b), to evaluate the effects of an extreme weather event on the ocean and coastal characteristics. The proposed methodology aims to the better understanding of the Medicanes' impact on the marine environment focusing on the improvement in the ability to predict their adverse effects on the coastal zone.

The storm surge events, related to Medicanes during the last decade, are more intense than those produced by the main seasonal storms, thus affecting the coastal vulnerability in terms of both erosion and flooding (Bakkensen 2017; Scicchitano et al. 2021). Androulidakis et al. (2015) and Makris et al. (2016, 2023) showed that the magnitude of storm surges may increase in several Mediterranean sub-regions, mainly during the first half of the twenty-first century. Future projections show that the greatest storm surges may occur in the Adriatic Sea and in regions characterized by wide and mild sloping continental shelves (Toomey et al. 2022). The effect of winds and inverse barometer on storm surges reveals a strong spatial variability. Even though the sea-level pressure (SLP) is a strong contributor to the sea-level anomaly (SLA) peaks over the Ionian Sea during a storm, the wind effect and the respective accumulation of water masses along the Ionian coasts are the main factors that influence the storm surges similarly to the rest of the Adriatic Sea coasts (Orlic et al., 1994; Vilibić, 2006; Pirazzoli and Tomasin 2002; Lionello et al. 2006, 2019; Marcos et al. 2009; Krestenitis et al. 2011; Androulidakis et al. 2015; Šepić et al. 2015; Međugorac et al. 2018; Tolika et al. 2021). During Medicanes, the flooding penetration over the land, associated with the accompanying storm surges, can be larger than the penetration caused during typical storms; the Medicanes Qedresa (2014) and Zorbas (2018) showed overland flood extents larger than 100 m from the shoreline, while typical storms normally cause inland inundation that does not extend more than 50 m from the coast in regions of southeastern Sicily (Scicchitano et al. 2021).

Medicanes reveal a low annual frequency (~1.1 events/year in Miglietta et al. 2013; ~1.6 events/year in Cavicchia et al. 2014; 1.4 events/year in Nastos et al. 2018) and evolve mainly in the western and central Mediterranean, especially between the Ionian Sea and the northern African coast. Medicanes exhibit a seasonal cycle of a higher frequency in the autumn–winter period with a peak in the beginning of winter and of lower frequency over spring and summer (Cavicchia et al. 2014; Nastos et al. 2018). The increased sea surface temperature (SST) trends during the last decades over the Mediterranean Sea (Pisano et al. 2020; Darmaraki et al. 2019; Androulidakis and Krestenitis 2022) that are related to the human influence on climate, formed more favorable conditions (warmer water pools), strengthening the intensity of Medicanes. Future SST increasing trends, derived from projected climatic scenarios over the Mediterranean Sea during the last decades of the twenty-first century, may also result to stronger and longer lasting Medicanes than today (Miglietta et al. 2011; Pytharoulis et al. 2018). SST state has a minor influence on the track, but a strong effect on the intensity (Noyelle et al. 2019) and lifetime (Pytharoulis 2018) of Medicanes. Romero and Emanuel (2013) concluded that the climate change due to global warming is expected to increase their intensity, but not their frequency. One of the warmest years with respect to the SST over several Mediterranean Sea areas was 2020 (Androulidakis and Krestenitis 2022). Medicane IANOS was formed and propagated over the central Mediterranean in mid-September 2020, when the SST anomaly revealed higher levels (>2 °C) than the SST climatology

(Lagouvardos et al. 2021). The storm surge formation of IANOS from its generation until its evolution over the western coastal Greece is under evaluation in this study.

IANOS was formed over the central Mediterranean Sea during September 15–20, 2020 (Lagouvardos et al. 2021; https://marine.copernicus.eu/news/following-cyclone-ianos-across-mediterranean-sea), characterized by conditions similar to a Category 2 Hurricane in the Saffir–Simpson scale (1-min sustained winds up to 159 km/h), and Medicane-induced damages were observed in both inland and coastal areas, especially in the central and southwestern Greece, causing extensive flooding, infrastructure destructions, and four human casualties. Intense storm surges produced inundation phenomena over lowland elevation areas, mainly along the western coasts of Greece in the Ionian Sea (Fig. 1a). In this paper, we investigate the flooding conditions over the affected coastal regions during the IANOS passage.

Our approach consisted of several coupled components: atmospheric simulations to provide meteorological forcing to the ocean hydrodynamic modeling (simulation of barotropic circulation and storm surges), tide-gauge measurements for model validation, satellite ocean color observations, and coastal inundation modeling for the estimation and mapping of flooding in coastal lowland plains (Fig. 1b). The sea-level conditions and characteristics during the IANOS passage over the affected coastal regions are investigated with the use of a two-dimensional (2-D) hydrodynamic model for barotropic circulation, operating in both forecast (Operational System Wave4us; http://wave4us.web.auth.gr/; Krestenitis et al. 2017) and hindcast (Androulidakis et al. 2015) modes (Fig. 1b). Herein, even though the baroclinic conditions are a very important component of the general circulation in the Mediterranean Sea, we focus on the sea-level response due to severe meteorological conditions (barotropic component) that largely determined the ocean circulation and coastal sea-level variability during a severe low-pressure system (IANOS Medicane in September 2020). The first goal of the study was to examine the variability of the meteorological effects on the distribution of the accompanying storm surges during IANOS along the affected coasts of the central Mediterranean. Based on field observations, we evaluate the performance of our forecast system to efficiently predict the storm surge levels over the coastal zone during the passage of an exceptionally intense cyclonic system. We also test the improvement in the simulations using higher-resolution meteorological forcing (in hindcast mode; Fig. 1b). The second goal was to estimate the coastal inundation characteristics in specific coastal areas and evaluate two different flooding detection techniques based on satellite imagery and numerical modeling (Fig. 1b). Differences among the coastal areas, associated with the response of the sea-level evolution during the storm passage, are also identified.

Following the introductory section, Sect. 2 describes the methods and the observational field and satellite data used in the study (detailed descriptions of the coastal flooding methods are provided in Appendices A and B). Section 3 presents the evaluation of the storm surge simulations with the use of field measurements. The marine weather conditions during IANOS Medicane are analyzed in Sect. 4. The storm surge variability along the coastline, the effects of atmospheric conditions on coastal sea level, and the estimation of the coastal inundation are presented in Sect. 5. The study's results are discussed in Sect. 6, and the main concluding remarks are presented in Sect. 7.

2 Methods and data

2.1 Numerical models

A series of numerical models with different spatial resolutions are combined, in one-way coupled mode (Fig. 1b), to simulate the meteorological conditions over the Mediterranean Sea (synoptic scale; Sect. 2.1.1), the ocean circulation effects, i.e., the storm surge variability in the central part of the basin (regional scale; Sect. 2.1.2), and the flooding processes over the affected coastal areas (local scale; Sect. 2.1.3). The coupled numerical simulations during the IANOS period are described in Sect. 2.1.4.

2.1.1 Meteorological conditions

The meteorological conditions are derived from two sources. The first one includes the operational numerical weather predictions (NWP) of the Laboratory of Meteorology and Climatology of the Aristotle University of Thessaloniki (LMC-AUTH), Greece, and the second one is the gridded operational analyses of the European Centre for Medium-range Weather Forecasts (ECMWF). These fields were employed in forecast and hindcast mode simulations of the storm surge (Sect. 2.1.2), respectively. The detailed setup of the two modes is described in Sect. 2.1.4.

The regional NWP were produced by the operational forecasting system of LMC-AUTH (Pytharoulis et al. 2015a, b; http://meteo.geo.auth.gr) that was originally developed and evaluated in the framework of Wave4us project (http://wave4us.web.auth.gr/). It is based on the Weather Research and Forecasting model with the Advanced Research dynamic solver (WRF-ARW, version 3.5.1; Skamarock et al. 2008; Wang et al. 2014). The NWP system consists of three nested domains that cover the northern Africa and most of Europe, including the whole Mediterranean and the Black Sea, with a grid increment of 15 km. The WRF-ARW model employs 39 sigma levels up to 50 hPa, with their highest density in the lowest troposphere. The instantaneous mean SLP and the 10-m zonal and meridional wind components at 3-hourly intervals are used in the forecast mode storm surge simulations of this study. The original forecast fields have been re-gridded to a $0.15^\circ \times 0.15^\circ$ (latitude–longitude) grid that covers the Mediterranean Sea, through bilinear interpolation. The forecast horizon is 96 h (4 days), and the model is initialized daily at 1200 UTC.

The ECMWF operational analyses of the atmospheric model were available for August and September 2020 at a horizontal grid spacing of $0.1^\circ \times 0.1^\circ$ for the whole Mediterranean basin. The analyses were produced at 6-h intervals by the data assimilation of the Integrated Forecasting System of ECMWF and particularly by its cycle 47r1. The mean SLP and the 10-m zonal and meridional wind components have been utilized in this study to force the hindcast mode of the ocean hydrodynamic simulations (see Sect. 2.1.4).

2.1.2 Storm surge model

The numerical simulation of the barotropic hydrodynamics is based on the high-resolution storm surge (HiReSS) numerical model developed in the Laboratory of Maritime Engineering in AUTH (de Vries et al. 1995; Krestenitis et al. 2011; Androulidakis et al. 2015; Makris et al. 2016; 2019). HiReSS simulates the 2-D barotropic mode of the hydrodynamic circulation in large water bodies, enclosed seas, gulfs, and coastal areas over a shoaling

continental shelf, based on the shallow water equations. Thus, it can predict the SLA and the depth-integrated sea currents (induced by atmospheric forcing; wind and SLP) combined with astronomical tide effects (Krestenitis et al. 2015; Makris et al. 2021a). The HiReSS model is the numerical forecast tool of several operational applications in regional and marginal seas (e.g., Mediterranean Sea, Red Sea, Yellow Sea, Black Sea, Java Sea, NW Atlantic Ocean), gulfs, straits, and local aquatic bodies (e.g., Gulf of Finland, Osaka Gulf, Tokyo Gulf, Persian Gulf, English Channel). These applications are operating daily and were created in the framework of two research projects: Wave4Us (Krestenitis et al. 2015; 2017; http://wave4us.web.auth.gr/; https://www.meteo.gr/meteomaps/sea_level.cfm) and Accu-Waves (Makris et al. 2021a; b; https://accuwaves.eu/forecast/). HiReSS model has also been used to estimate both future projections of storm surges under climatic scenarios (Androulidakis et al. 2015; Makris et al. 2016, 2023) and storm surge variability along coasts during past periods (Krestenitis et al. 2011). HiReSS can take into account the combinatory effects of several processes, such as the inverse barometer (response of sea level to atmospheric pressure gradient of large barometric systems); shear stresses of wind applied on the air–sea interface; geostrophic Coriolis forces on large water masses; astronomical tides; ocean bottom friction; turbulence of horizontal vortices through the eddy viscosity concept; impacts of the wave-induced mean flows (Stokes drift) on the wind-driven currents in open seas; additional sea surface setup caused by wave breaking in nearshore coastal zones; etc. In particular, HiReSS implementation in the Mediterranean Sea considers the effects of astronomical tides on barotropic circulation through a static model parameterization (Schwiderski 1980), following a formulation that combines the equilibrium tidal potential with the self-attraction/loading effect under specific coefficient parameterizations (Matsumoto et al. 2000; Sakamoto et al, 2013). Further description of the mathematical equations and thorough validation of the HiReSS implementation in the Mediterranean Sea with the use of satellite and field observations can be found in Krestenitis et al. (2011, 2015, 2017), Androulidakis et al. (2015), and Makris et al. (2016, 2019, 2021a, 2023).

2.1.3 Coastal inundation model

Depending on the desired level of complexity, the choices of existing models for 2-D flood simulations developed by the numerical hydraulics community for coastal inundation, too, are numerous. Among them, classic primes are MIKE FLOOD 2-D (e.g., Ballesteros et al. 2018), the Coastal Storm Modeling System (CoSMoS; Barnard et al. 2014; O'Neill et al. 2018), the coastal flood modules of the Advanced Circulation (ADCIRC) and Hydrologic Engineering Center-River Analysis System (HEC-RAS) 2-D models (e.g., Colle et al. 2008; Pandey et al. 2021), LISFLOOD-FP (Bates and De Roo 2000; Bates et al. 2005; 2010), and AutoRoute (Praskievicz et al. 2020).

Herein, we use CoastFLOOD, which is also an AUTH in-house numerical model for the simulation of coastal inundation hydrodynamics on a local scale over selected areas of the littoral land zone in Greece (Makris et al. 2020; Bates et al. 2005, 2010). The latter pertain parts of urban environment and engineered waterfronts, ports and coastal structures, agricultural plains, estuaries, adjacent lagoons, and natural beaches (Skoulikaris et al. 2021). The model is one-way coupled to HiReSS model (see Sect. 2.1.2), fed with output from simulated sea-level data as boundary conditions of its computational domain representing the floodwater hydraulic load on the study area's coastline. Hence, it provides estimations of possible extended flooding of lowland coastal areas, rural plains, farmlands, urban sites, deltaic regions, and

estuaries due to storm surges. CoastFLOOD model also incorporates a "static-level" inundation module operating in "Bathtub" mode (identifying lowland cells with ground elevation $z < SLA_{max}$, i.e., the maximum storm surge water level; Didier et al. 2019; Schmid et al. 2014) and an enhanced bathtub approach with hydraulic connectivity ("Bathtub HC" mode; Karamouz and Fereshtehpour 2019; West et al. 2018). Further information about the model's configuration is provided in Appendix A.

2.1.4 Hydrodynamic numerical simulations

The numerical simulations of storm surges are implemented in two modes: (1) forecast mode and (2) hindcast mode (Fig. 1b). The forecast mode is a module of the Operational System Wave4us (http://wave4us.web.auth.gr/; Krestenitis et al. 2017) that provides 3-day predictions of SLA fields and barotropic currents daily, over the entire Mediterranean Sea ($0.15° \times 0.15°$). The bathymetric input was derived from the General Bathymetric Chart of the Oceans (GEBCO; https://www.gebco.net/). The meteorological forcing (SLP and wind fields) of the forecast mode is derived from the operational WRF-ARW simulations with the same resolution over each domain and a 3-hourly time step (see Sect. 2.1.1). In this study, we use the first forecast day (12th to 33rd forecast hours to exclude the model spin-up time) that covers the IANOS track to evaluate the prediction performance of the storm surge in September 2020. Numerical simulations in a hindcast mode have also been conducted covering two successive months (August–September 2020) with meteorological forcing derived from the ECMWF operational analyses (see Sect. 2.1.1) to improve the HiReSS model's predictability. The first month (August) was used as a simulation warm-up period and the second month (September) provided the circulation fields covering the IANOS storm period. The storm surge model outputs from both simulations were compared and validated with available field observations along the Medicane's pathway (see Sects. 2.2.1 and 3).

The hourly output of simulated SLA, derived along the coastal area during the period of high IANOS storm surges, was used to feed the coastal inundation simulations with CoastFLOOD model over selected littoral zones (see Sect. 2.1.3 and Appendix A). The latter were identified as impacted areas detected by the satellite imagery technique (see Sect. 2.2.3 and Appendix B). The model's computational grid with land elevations was derived from a high-resolution (2 m) digital elevation model (DEM), described in Sect. 2.2.2. HiReSS model output of sea level on the coastline was used to force the CoastFLOOD model on its coastal land limit (shoreline). The used Dirichlet-type boundary conditions refer to local SLA-z (z: land elevation of raster cell) values. CoastFLOOD was implemented in three modes: (i) by a static Bathtub approach, (ii) as an enhanced Bathtub HC model, and (iii) in full flood routing mode by a 2-D horizontal, Manning-type hydraulic flow over the floodplain terrain (see Sect. 2.1.3 and Appendix A). Only steady-state inundation situations are considered herein, i.e., referring to an eventually constant sea-level boundary condition of storm surge maxima (SLA_{max}) for the timespan of storm-induced high seas on the coastline during the Medicane.

2.2 Observational data

2.2.1 Tide-gauge measurements

Field measurements of sea elevation have been collected by available tide-gauge sensors along the coasts of the Ionian and Aegean Seas. These measurements are freely provided by the Sea Level Station Monitoring Facility of the Intergovernmental Oceanographic

Commission (IOC/UNESCO; https://www.ioc-sealevelmonitoring.org/). The SLA time series with 1-min time step for eight stations (Fig. 1a) were derived for one month (September 2020) subtracting the estimated offset for each station to compute the surface variation around the mean sea level. The measured data are used to validate the performance of the numerical hydrodynamic simulations and estimate the realistic storm surge intensity during IANOS Medicane.

2.2.2 Land elevation data

Land elevation data were derived by post-processing of available geospatial data from the DEM of the official Greek service for comprehensive recording of real estate and property's metes-and-bounds, i.e., the Hellenic Cadastre (https://www.ktimatologio.gr/en). This DEM has a pixel size of 2 m and is available in 4600 × 3600 m ground plates, with a perimeter overlay of 300 m, in GGRS87 projection. The geometric accuracy of the DEM is less than 0.70 m, while its absolute accuracy is less than 1.37 m with a 95% confidence level (Chrisafinos and Kavvadas 2016). The selected DEM fields cover the coastal regions of the Ionian Sea. Rasterized versions of them were used to identify the affected lowland areas, serving also as input for the computational grid formulation of the CoastFLOOD simulations (see Sect. 2.1.3).

2.2.3 Satellite observations

Two types of satellite data were used in the study. The first type includes ocean color images collected by the Sentinel-2 satellite to estimate the coastal inundation during the IANOS Medicane. The resolution of the Sentinel-2 images is 10 m, and they are freely provided by the Earth Explorer application operated by the United States Geological Survey (USGS; https://earthexplorer.usgs.gov/; latest access on March 20, 2022). The Sentinel-2 raster images were used to compute the Normalized Difference Water Index (NDWI; Gao 1996) over specific coastal regions that were severely affected by the storm. The NDWI is broadly used to monitor changes related to water content in water bodies (McFeeters 1996). Underwood et al. (2012), Kalcic et al. (2012), and Ogashawara et al. (2013) used ocean color imagery and NDWI computation, derived from MODIS and LANDSAT-5 satellites, to assess the flooding conditions due to storm surge phenomena related to hurricanes in the northern Gulf of Mexico. The NDWI approach is capable of clearly separating land and water, and can be also used for coastline analysis (Anggraini et al. 2018). Herein, we use the NDWI and Quantum Geographic Information System (QGIS; https://qgis.org/) mapping and analysis to estimate the hydrological conditions of the land (i.e., if land cells are dry or wet after a storm surge event). This is the first attempt to our knowledge that uses NDWI to estimate the surge-induced coastal flooding in the Mediterranean Sea. Detailed description of the NDWI derivation method is provided in Appendix B.

The second type of satellite data includes the sea surface temperature (SST) set, distributed by the E.U. Copernicus Marine Service (https://www.copernicus.eu/), covering the entire IANOS period (15/9–20/9; latest access on November 20, 2021). The satellite-derived data consist of daily mean, gap-free (L4) horizontal fields (Nardelli et al., 2019) at high spatial resolution (0.01°) over the Mediterranean Sea. Remotely sensed L4 SST datasets are operationally produced and distributed in near-real time by the Consiglio Nazionale delle Ricerche—Gruppo di Oceanografia da Satellite (CNR-GOS). The Mediterranean SST data were used to analyze the SST temporal and spatial variability over

the IANOS-affected area and to describe the sea surface conditions before and during the IANOS formation and propagation.

3 Evaluation of storm surge simulations

Extensive validation of the HiReSS model performance that has been conducted in various previous applications in the Mediterranean Sea (Krestenitis et al. 2011, 2015, 2017; Androulidakis et al. 2015; Makris et al. 2016, 2019, 2021a, 2023), confirmed the ability of the model to simulate the barotropic circulation and sea-level elevation due to meteorological conditions. Herein, the model's efficiency in simulating the storm surges specifically during the IANOS event and over the most affected regions under both forecast and hindcast modes is under evaluation.

The statistical measures and model performance skill metrics used in the study refer to the entire time series of SLA (both modeled and observed) during the period of September 2020, leading up to the IANOS event until its passage. We calculated the root-mean-square error (RMSE) of SLA between modeled and observed values in each of the eight selected stations, located in the Ionian and Aegean Seas (Fig. 1a). The percentage index of the ratio RMSE/SLA_{max} (SLA_{max} corresponds to the maximum SLA value of the tide-gauge observations) is also estimated, followed by the classic Pearson product-moment correlation coefficient (R_p), i.e., the covariance of the modeled and observed SLA variables divided by the product of their standard deviations. R_p coefficient (≤ 1, 1 being the full agreement between modeled and observed SLA) measures the strength of linear dependence between experimental and numerical data but does not directly compare their actual values. Therefore, the combination with the RMSE provides a clearer insight on the HiReSS model performance skill. Moreover, the Willmott skill score (W_S) or Index of Agreement (Willmott et al. 2012) is also calculated for SLA. Higher W_S values (≤ 1 as limit) reveal a better match between simulated values of SLA and observations by tide gauges, while W_S values close to 0 indicate disagreement between the two samples.

The mean daily SLA revealed the highest levels during the IANOS event, specifically between 17/9 and 18/9 depending on the location of the station (Fig. 2). During the northeastward propagation of the storm (see Sect. 4.1), it firstly affected the Catania (Fig. 2a) and Otranto (Fig. 2f) areas in southern Italy on 17/9. The eastward turn of the storm over the Ionian Sea on 18/9 increased the sea elevation as measured by all tide gauges located at the western Greek coasts (Fig. 2c, d, e). The forecast mode of the model showed a better performance over the Ionian Sea than in the initial phases of the Medicane event during the storm's propagation closer to the Italian coasts. This difference is mainly associated with uncertainties of the operational WRF-ARW forcing in the early stages of the storm (see Sect. 4.1). The atmospheric forcing derived from the ECMWF fields improved the storm surge simulation (hindcast mode) over almost all areas. The correlation coefficients (R_P) between the hindcast-simulated data and field observations ranged between 0.62 and 0.86 with smaller RMSEs in comparison with the forecast simulations (Table 1). All correlations coefficients are statistically significant ($p_{values} < 0.0001$), based on the Mann and Kendall (MK; Mann 1945; Kendall 1975) test (p_{value} less than 1% indicates a statistically significant correlation). The median value of all R_P increased from 0.67 (forecast mode) to 0.75 (hindcast mode) and the RMSE/SLA_{max} improved by 8% with the use of the improved ECMWF forcing. The overall correlation coefficient and coefficient of determination, using all measurements, are

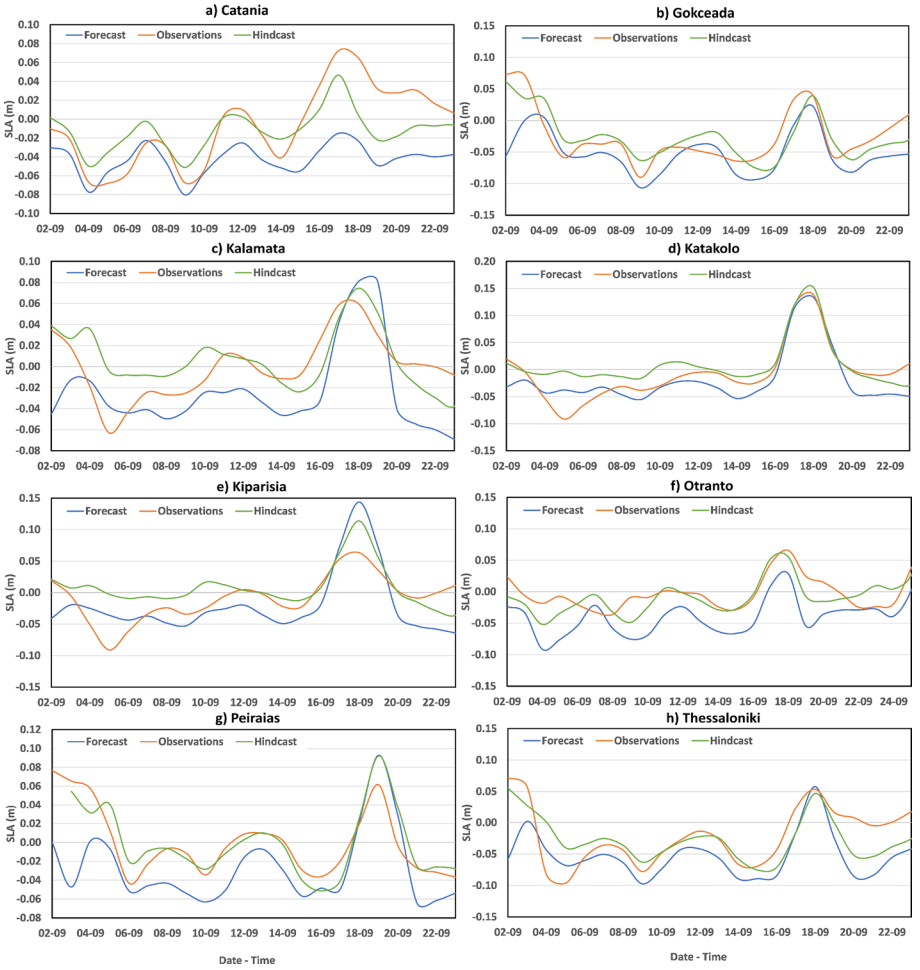

Fig. 2 Comparisons of mean daily sea-level anomaly (SLA; m) by HiReSS model results in forecast (blue line) and hindcast (green line) modes against field data of tide-gauge observations (orange line) for the IANOS period between September 2 and 23, 2020, at eight stations (Fig. 1): **a** Catania, **b** Gokceada, **c** Kalamata, **d** Katakolo, **e** Kyparissia, **f** Otranto, **g** Peiraias, and **h** Thessaloniki

more than 0.7 and 0.5 in the hindcast mode, respectively (Fig. 3b). The two correlation coefficients (Fig. 3a and b), using all station data, are statistically significant with $p_{values} < 0.0001$. Most of the SLA_{mod}–SLA_{obs} pairs are aligned along the $(x = y)$ identity line in both simulations with a clear improvement for the hindcast mode. The W_S skill score is improved in the hindcast mode, reaching very high values in both Ionian (Table 1; e.g., Katakolo: $R_P = 0.90$; RMSE = 0.03 m) and Aegean regions (Table 1; e.g., Gokceada: $R_P = 0.94$; RMSE = 0.026 m). It is concluded that the quality of the atmospheric forcing is a determining factor of the ocean model predictability for storm surges. Although the usage of ECMWF fields as meteorological forcing of the HiReSS significantly improved the SLA simulations (hindcast mode), the forecasts conducted by the operational system (WRF/ARW-fed HiReSS simulations) provide useful real-time daily predictions that improve in time, as they are forced by daily updated meteorological

Table 1 Validation of HiReSS model performance in hindcast and operational forecast modes (left and right columns, respectively) against field observations, based on statistical measures and skill metrics (Pearson's correlation coefficient: R_P, root-mean-square error: RMSE, Willmott skill score: W_S) for the sea-level anomaly (SLA) during September 2020 at eight selected stations (Fig. 1a)

Validation sites		ECMWF-fed HiReSS in Hindcast mode			WRF/ARW-fed HiReSS in forecast mode		
A/A	Station	Pearson correlation R_P	RMSE SLA (m)	Willmott skill score W_S	Pearson correlation R_P	RMSE SLA (m)	Willmott skill score W_S
1	Catania	0.79	0.028	0.80	0.72	0.047	0.40
2	Gokceada	0.80	0.026	0.94	0.70	0.042	0.89
3	Kalamata	0.63	0.025	0.80	0.64	0.039	0.65
4	Katakolo	0.86	0.030	0.90	0.87	0.028	0.92
5	Kyparissia	0.62	0.034	0.75	0.66	0.039	0.76
6	Otranto	0.73	0.021	0.86	0.64	0.044	0.50
7	Peiraias	0.70	0.027	0.83	0.66	0.041	0.67
8	Thessaloniki	0.71	0.033	0.91	0.65	0.049	0.84
Statistics		Maxima of: $R_P=0.86$, $W_S=0.94$ Median of: $R_P=0.75$, $W_S=0.85$ Minima of: RMSE SLA = 0.021 m, RMSE/SLA$_{max}$ = 12.6%			Maxima of: $R_P=0.87$, $W_S=0.92$ Median of: $R_P=0.67$, $W_S=0.72$ Minima of: RMSE SLA = 0.028 m, RMSE/SLA$_{max}$ = 20%		

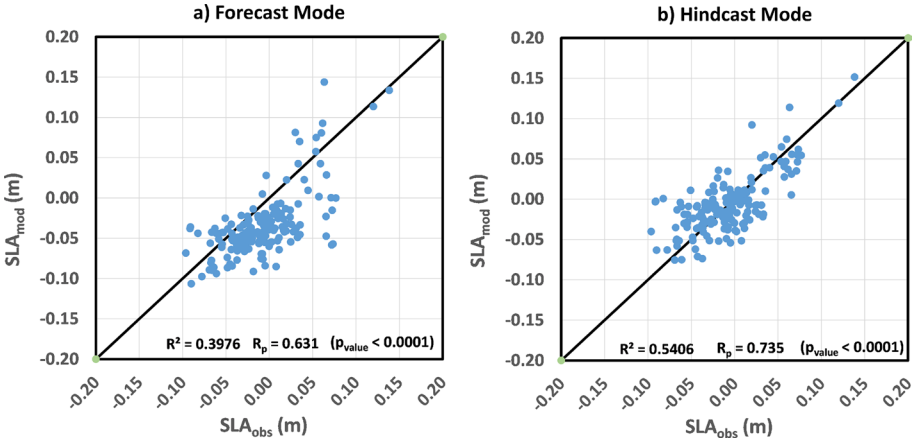

Fig. 3 Scatter diagrams of comparisons between HiReSS-modeled sea-level anomaly (SLA; m) and field data of tide-gauge observations (SLA_{mod} and SLA_{obs}, respectively) at eight selected stations (Fig. 1a) for September 2020; **a** WRF/ARW-fed HiReSS model results in operational forecast mode; **b** ECMWF-fed HiReSS model results in hindcast mode. The Pearson correlation coefficients (R_P), the respective p_{values} from the MK test of statistical significance, and the coefficients of determination (R^2) are shown

forecasts. Hereafter, the rest of the analyses are based on simulated ocean data derived from the hindcast mode of the model (ECMWF-fed HiReSS simulations).

The highest SLA ($SLA\ Max_{Obs}$ = 0.27 m; $SLA\ Max_{Model}$ = 0.29 m) was measured in Katakolo (west Peloponnesus; Fig. 1a) on 18/9 00:00 UTC (Fig. 4a). The core of the IANOS Medicane was over Cephalonia and Zakynthos islands on 18/9 00:00, with very strong cyclonic winds (> 20 m/sec) blowing toward the coast of Peloponnesus (Fig. 4b). The onshore wind field accumulated water masses strengthening the storm surges along the

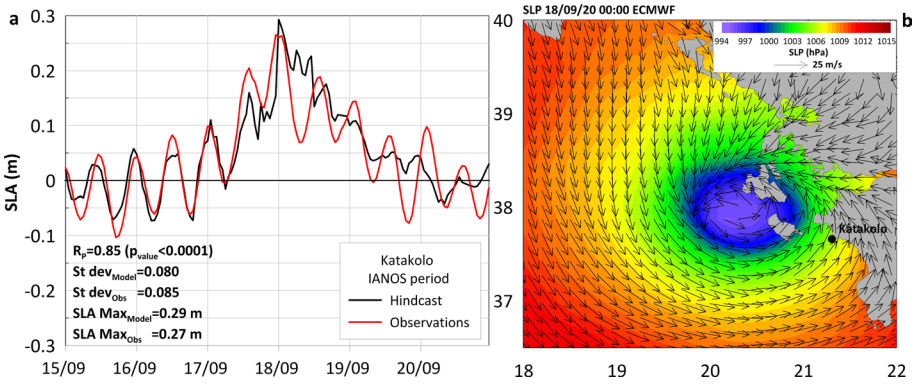

Fig. 4 **a** Variation of sea-level anomaly (SLA; m) with hourly time step derived from the hindcast simulation (black line) and the observed data (red line) at Katakolo (west Peloponnesus) during the IANOS passage (15/9–20/9) in the Ionian Sea. The Pearson correlation coefficient (R_P) with the MK test of statistical significance (p_{value}), the standard deviation (St dev) and the SLA maximum value (SLA Max) from simulated and observed time series (6 days) are shown. **b** Map of 2-D horizontal distributions of sea-level pressure (SLP; hPa) and winds (vectors; m/s), derived from ECMWF, over the broader region around Katakolo in the south-central Ionian Sea at the time of maximum SLA (18/9/20 00:00)

western coasts. The variability of atmospheric conditions' impact on storm surges is discussed in Sect. 5.1. The hourly modeled SLA variation, derived from the HiReSS hindcast mode, proves to be an efficient simulation of the actual storm surge, realistically reproducing the tidal oscillations over this area ($R_P = 0.85$ with 142 degrees of freedom and MK test: $p_{value} < 0.0001$). The standard deviation of the simulated SLA (St dev_{Model}) during the IANOS period (15/9–20/9) is around 8 cm, approximately the same as the respective value derived from the field data time series (St $dev_{Obs} = 8.5$ cm). The reported storm surges at the coasts of the Ionian Sea are confirmed by the increased observed and simulated SLA on 18/9, when the landfall of IANOS took place on the central coastal region.

4 Analysis of marine weather conditions

4.1 Meteorological conditions during IANOS

The actual track of the IANOS Medicane over the south-central Mediterranean Sea, derived through the combination of MeteoSat Second-Generation satellite imagery and NCEP Final Operational Global Model analyses (FNL with a grid spacing of $0.25° \times 0.25°$), has been reported (Fig. 5c) by Lagouvardos et al. (2021). The northeastward pathway during the 15/9–17/9 period, the eastward turn toward the central Ionian Sea after 17/9, and the southeastward shift of the storm after its landfall on western Greece toward the northern African coasts have been efficiently reproduced by both WRF-ARW operational forecasts (Fig. 5a) and ECMWF analyses (Fig. 5b). The track derived from the ECMWF fields (Fig. 5b) agrees with the estimation showed by Lagouvardos et al. (2021; Fig. 5c) who combined a different global analysis product (NCEP/FNL) and satellite data. Small differences are identified in the forecast mode (Fig. 5a), especially in the initial formation phases of the storm. The SLP reduction (< 1000 hPa) was slightly underestimated by WRF-ARW (Fig. 5a), predicting a weaker storm (higher SLPs) than ECMWF analyses (Fig. 5b) on 16/9. However, the overall track and intensity of the cyclone, especially after the storm's eastward shift toward Greece on 17/9, were well reproduced by the daily forecasts confirming the ability of the WRF-ARW to predict the evolution of Medicanes in operational forecast mode. The cyclonic winds of IANOS followed the pathway of the storm (Fig. 5f, i, l), showing stronger values (> 20 m/sec) over the Ionian Sea after 17/9 (Fig. 5i). The Medicane affected the wind distribution of the broader central Mediterranean Sea with northwesterly winds prevailing over the Adriatic Sea, westerly winds over the Libyan Sea and Gulf of Sidra, and southwesterlies between Peloponnesus and Crete. The cyclonic winds have also affected the weather state of the eastern Aegean Sea on 18/9 (Fig. 5l), inducing though lower storm surges than the main affected region of the Ionian Sea (Fig. 5k; see Sects. 4.2 and 5.1). IANOS "eye" made landfall on the central Ionian region on 18/9 00:00 (Fig. 5b and 5c) inducing strong onshore winds toward the southern Ionian coasts (Fig. 5l).

In the early hours of 18/9, the meteorological stations of the Hellenic National Meteorological Service at the airports of Cephalonia and Zakynthos islands recorded maximum wind gusts of 30.9 m/s (111.1 km/hr; SYNOP reports). The maximum recorded 1-min wind speed and wind gust reached 44.1 m/s and 54.2 m/s, respectively, at Palliki, Cephalonia (about 20 km north of the airport) on 18/09 (Lagouvardos et al. 2021). The SLP at the airport of Cephalonia dropped to 994 hPa (METAR reports) at 05:50 UTC on 18/09. It is noted that at this station the METAR reports were reported only from 05:50 to 18:50 UTC, at hourly intervals. Lagouvardos et al. (2021) showed that an even lower SLP of

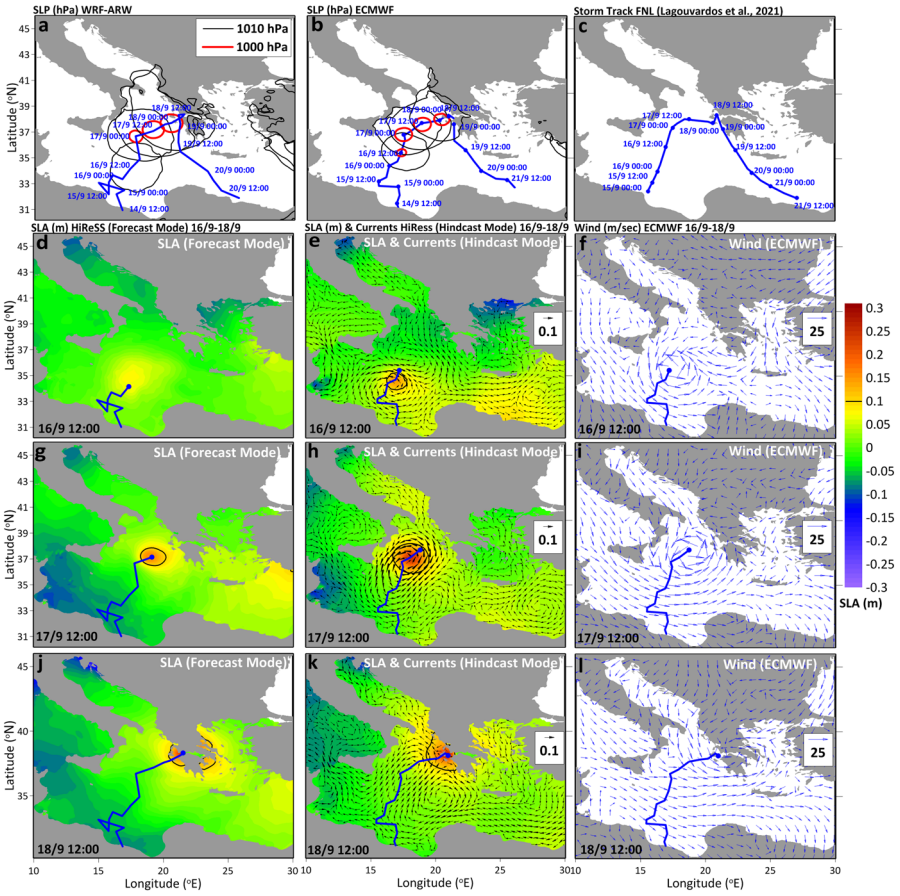

Fig. 5 Evolution of 1010 hPa (black line) and 1000 hPa (red line) isobaric contours (by sea-level pressure, SLP) derived from the **a** WRF-ARW forecasts, and **b** the ECMWF analyses (12-h step). **c** Storm track, derived by Lagouvardos et al. (2021) from the Final Operational Global Analysis of the National Center for Environmental Prediction (NCEP FNL) database and MeteoSat Second-Generation satellite imagery. Snapshots of sea-level anomaly (SLA; m) derived from the HiReSS simulations in (d, g, j) forecast and (e, h, k) hindcast modes, and the respective (f, i, l) wind fields (m/sec) from ECMWF dataset on 16/9 12:00, 17/9 12:00, and 18/9 12:00. The SLA = 10 cm is marked with black contours in the SLA maps. The vector maps of the barotropic currents (m/sec; hindcast mode) for the same dates are superimposed over the SLA hindcast snapshots. The tracks (6-h step) of WRF-ARW and ECMWF are overlaid in panels (a, d, g, j) and (b, e, f, h, i, k, l), respectively (blue lines)

984.3 hPa was measured at Palliki, Cephalonia, at about 02:00 UTC on 18/09. These measurements reveal the intensity of IANOS, while its minimum SLP is among the lowest values recorded in Medicanes (Miglietta et al. 2013; Pytharoulis 2018; Cioni et al. 2018).

4.2 Ocean response during IANOS

A storm-induced barotropic cyclonic eddy (anticlockwise currents) was formed below the "eye" of IANOS, moving northeastward along the storm's track (Fig. 5e and h). The

eddy finally made landfall on the western coasts of Greece on 18/09 (Fig. 5k). The SLA is around 0.1 m, below the storm on 16/9, and increased to 0.25 m, 1 day later at the area between Italy and Greece (Fig. 5h). Weaker (lower sea level) and topographically narrower storm surges were estimated in the forecast mode of the model (Fig. 5d, g, j) in comparison with the sea-level increases, derived by the hindcast simulations (Fig. 5e, h, k). This result agrees with the coastal comparisons presented in Sect. 3. The cyclonic ocean currents inside the storm-induced eddy strengthened (> 0.1 m/sec), when IANOS moved between Sicily and Greece on 17/9 (Fig. 5h), forming onshore currents and enhancing the accumulation of water masses over the southwestern Greek coasts (see Sect. 5.1). The cyclonic currents due to the IANOS intrusion in the Ionian Sea also affected the barotropic circulation in the Adriatic Sea; the currents were reversed from southeastward (Fig. 5e) to northwestward (Fig. 5h) and increased the SLA in the northern part of the Ionian basin on 18/9 (Fig. 5k). The transition of the storm away from the African coasts after 16/9 reduced the sea elevation in the Gulf of Sidra (Fig. 5h). The landfall of IANOS on the central Ionian Islands and coasts with its core's SLP < 1000 hPa (Fig. 5b) increased the SLA over the broader Ionian region.

The evolution of the marine cyclone, defined by the 10-cm SLA contour, is shown in Fig. 6a. Several coastal regions of Libya revealed high sea levels on 15/9, and the well-formed SLA increase inside the cyclone followed a northeastward pathway on 16/9 (Fig. 6a). The currents inside the cyclone were stronger on 16/9 (0.02–0.04 m/sec), especially over the northern part of the eddy (Fig. 6b). The evolution of the storm between Sicily and Greece on 17/9 formed a large cyclonic eddy with strong barotropic currents at the periphery of the vortex (> 0.04 m/sec; Fig. 6b). A first SLA peak (0.3 m), derived from all SLA values inside the eddy, occurred in the night of 16/9 (Fig. 6c). The sea level varied among high values between 17/9 and half 18/9, when the storm reached the Greek coasts. The spatially averaged current velocities inside the eddy revealed the highest values on 17/9 (black line in Fig. 6d) when the maximum barotropic flow speeds also occurred (red line in Fig. 6d). The prevailing westward current component on 16/9 and 17/9 (negative values of the blue line in Fig. 6d) gradually reduced by 18/9, when the eastward component toward the Ionian coasts increased. The northward component (positive values of the green line in Fig. 6d) prevailed when the cyclonic eddy propagated in the Ionian Sea, but it was reduced when the storm made landfall on the coast on 18/9. The coverage area of the storm-induced eddy showed its highest extensions (Fig. 6e) simultaneously with the SLA peaks (Fig. 6c); the largest area of the eddy was computed in the afternoon of 17/9 (> 100,000 km^2; Fig. 6e), covering the entire region between southern Italy and western Greece (Fig. 6a). After the storm landfall on 18/9, the extension of the eddy reduced below 40,000 km^2, when the SLA values above 10 cm spread along the western coastline of Greece (Figs. 5k and 6a).

Significantly high SST levels have been recorded over the Gulf of Sidra on 15/9 (Fig. 7; > 29 °C), day and area of IANOS formation (Fig. 5c). Noyelle et al. (2019) suggested that the high SST levels enhance the tropical transition and thermodynamic intensification of Medicanes, similar to tropical storms. Very high SST prevailed before the IANOS propagation toward the Ionian Sea in agreement with Lagouvardos et al. (2021) who showed that the SST anomaly in the Ionian Sea on 15/9 was 2 °C higher than the daily SST climatology, forming a warm pool and creating favorable conditions for the generation of Medicanes. Prior to the formation of the Medicane, low temperature values were only detected in the Adriatic Sea (Fig. 7), and especially along its eastern coasts, under coastal upwelling processes due to the domination of northerly winds (Orlic et al. 1992) over the area (Fig. 5f). IANOS moved northward toward Sicily on 16/9 and the upwelling processes

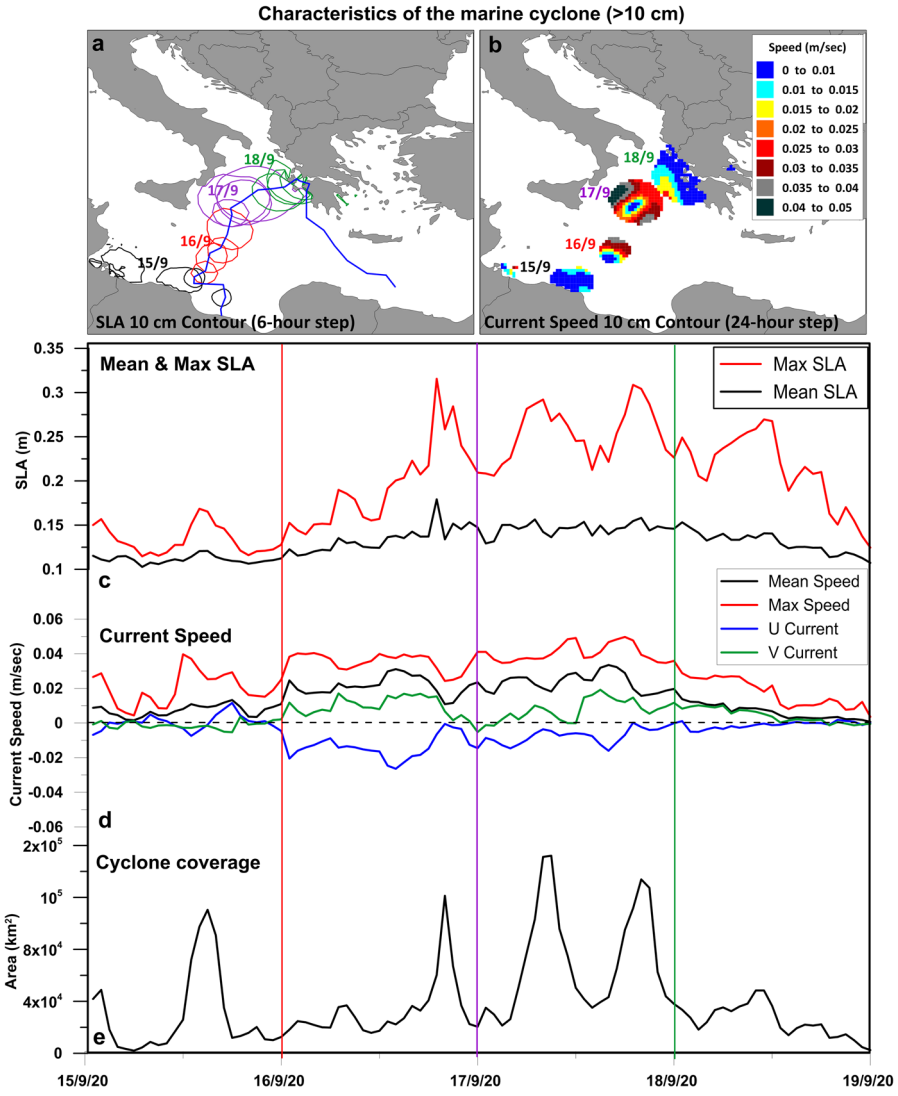

Fig. 6 Snapshots of **a** the 10-cm sea-level anomaly (SLA) contour (6-h step; starting at 00:00) and **b** distribution of barotropic current speed (m/sec) inside the respective contours (24-h step; starting at 12:00) from 15/9 to 18/9. Time series of **c** mean and maximum (Max) SLA, **d** mean, max, mean zonal (U), mean meridional (V) current speed, and **e** area of the marine cyclonic eddy (km^2), derived from the HiReSS simulation inside the 10-cm contour from 15/9 to 18/9. The color of the vertical grid lines, which indicate the beginning of each of the 4 days between 15/9 and 18/9, corresponds to the color of the respective closed contour lines shown in panel (a). The storm track derived from the ECMWF dataset is included in panel (a)

below the storm's core formed a cold wake along the track, associated with the cyclonic ocean eddy, revealing significant SST drops around 35°N–17°W (< 26 °C; Fig. 7). The anticlockwise barotropic currents of the eddy, responsible for the upwelling of the colder waters cover the area between the core of the storm and low SST signal on 16/9 and 17/9; colder waters spread over the area offshore of Sicily, following the southward bound along

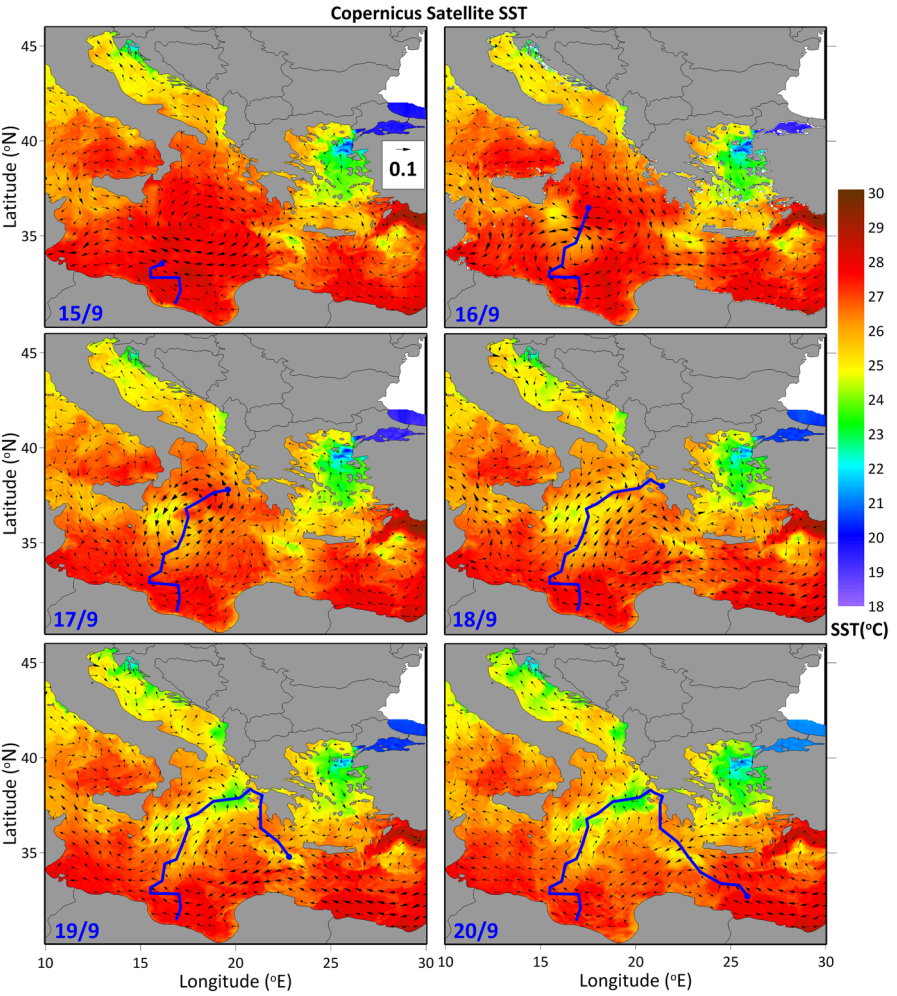

Fig. 7 Horizontal distribution of sea surface temperature (SST; °C) derived from the Copernicus satellite SST data overlaid by the barotropic currents derived from the HiReSS simulations from 15/9 until 20/9 of 2020 over the central Mediterranean Sea. The storm track derived from the ECMWF dataset and the location of the storm's eye (blue dot) at 18:00 of each day are also shown

the western side of the eddy during both days. The cold wake's signal is more evident at the southwest of Sicily on 17/9 and 18/9, and it is aligned along the IANOS track to the east between 19/9 and 20/9 (Fig. 7).

The distribution of the cyclonic-anticyclonic circulation conditions due to the IANOS impact is estimated based on the computation of the relative vorticity (RV) of the barotropic circulation, normalized by the Coriolis frequency (RV/f; Fig. 8a). The positive RV/f values along the Libyan coasts on 15/9 (8c) are associated with the cyclonic activity due to the IANOS formation. Almost the entire Gulf of Sidra is characterized by RV/f values higher than 2.5 (not shown), while the region north of the storm (~ 35°N)

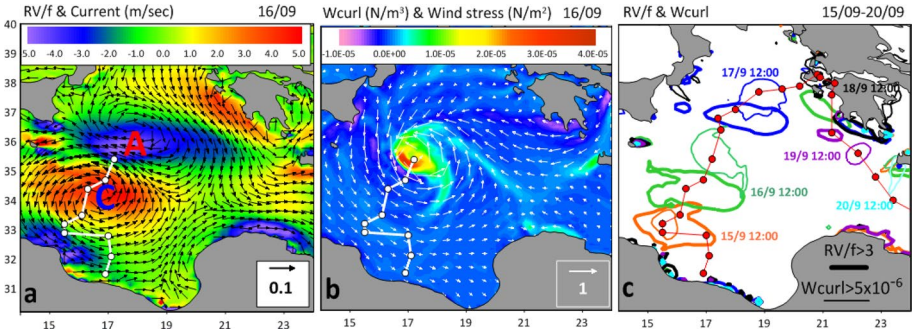

Fig. 8 **a** Relative vorticity normalized by the Coriolis frequency (RV/*f*), overlaid with barotropic currents, and **b** wind stress curl (Wcurl; N/m^3), overlaid with wind stresses, on 16/9 12:00, as derived from the HiReSS and ECMWF, respectively. **c** Overall daily (12:00) evolution of RV/f = 3 Wcurl characteristic contours from 15/9 to 20/9 (the contour lines surround values > 3 for RV/f and > 5×10^{-6} N/m^3 for Wcurl). The storm track derived from the ECMWF dataset and the locations of the storm's eye (dots) with 3-hourly step are also shown. The ocean anticyclonic (A) and cyclonic (C) circulation features are marked in (a)

was out of the cyclonic circulation pattern revealing high negative vorticity values; anticyclonic currents associated with the negative RV/f values were computed at the area northeast of the cyclonic eddy on 16/9 (Fig. 8a). The anticyclonic circulation was apparent and extended over the entire central Mediterranean before the formation of the Medicane (not shown) but the evolution of the marine cyclone at its southern boundary suppressed and shifted the anticyclone northward. The two count-rotating eddies (cyclone in the south and anticyclone in the north) induced strong westward currents over the tangential area (Fig. 5e) during the northward movement of the dipole as also confirmed by the current speed maps in Fig. 6b (e.g., on 16/9). This vorticity dipole moved northward along the storm's track on 16/9 and 17/9 (Fig. 8c), when, similar to the cyclone extension (Fig. 6a), positive RV/f values covered the entire region between Sicily and Greece. The core of the storm is located in the center of the dipole (between the two eddies; Fig. 8a); the water pool with cyclonic characteristics reveals an approximately 6-h lag after the storm's eye position showing that the stronger cyclonic currents are formed at the wake of storm. The highest values of the wind stress curl (Fig. 8b), associated with IANOS, precede the cyclonic eddy (Fig. 8a) in the open sea (e.g., 16/9 and 17/9; Fig. 8c). On 17/9, an elongated zone of cyclonic currents (high RV/f values; Fig. 8c) is observed south of the storm's eye, covering a large area between Sicily and Peloponnesus and inducing onshore currents toward the southern Ionian coasts (see Sect. 5.1). A positive vorticity belt was also computed along the southwestern coastline of Greece (Peloponnesus) on 18/9 characterized by onshore currents; this cyclonic belt shifted offshore after the removal of the storm away from the coast on 19/9. On 20/9, positive values related to the storm-induced cyclonic activity were detected only near Crete. It is noted that the strong and distinct cyclonic–anticyclonic dipole that evolved during the first days of the storm in the open sea, gradually attenuated when the storm reached the land, forming an elongated cyclonic stretch along the western Greek coasts (Fig. 8c).

5 Impacts on the coastal zone

The flooding impacts of the IANOS Medicane were mainly detected at the coasts of the central and southern Ionian Sea. We further studied the variability between the coastal storm surges and the effect of the different meteorological components related to the storm (SLP, wind speed, and direction), focusing on the most-impacted regions (Ionian and Aegean Seas; Sect. 5.1). The characteristics of the surge-induced coastal inundation were investigated based on satellite imagery, land elevation data, and numerical simulations (Sect. 5.2).

5.1 Storm surges along the coastline

The highest coastal sea elevations of September 2021 were detected along the Ionian Sea, especially around Cephalonia Island (0.25–0.30 m; Fig. 9a). These SLA peaks occurred due to the IANOS impact on the central and southern regions (Fig. 9b), while the northern Ionian's (e.g., Corfu) maximum SLA peaks (Fig. 9a) did not occur during the Medicane period (Fig. 9b and c). The 5-day (15/9–19/9) mean values were higher than 5 cm for the entire central region and positive for the rest of the Ionian (both north and south) with slightly higher values in Peloponnesus (Fig. 9d). The highest values of the entire Aegean coastline were not associated with the IANOS effects (Fig. 9c); the 5-day mean values were very close to the mean sea level during the entire Medicane period (Fig. 9d), while the maximum SLA values were lower than 10 cm (Fig. 9b).

The respective correlations between the coastal surge and the atmospheric components (pressure and wind) show both spatial (along the Ionian and Aegean coastline) and temporal (during and before/after IANOS) variability (Fig. 10). The Pearson coefficient between atmospheric pressure and sea level is negative and quite strong over the *N*. Aegean coasts ($R_{SLP} < -0.60$; Fig. 10a) associated with the inverse barometer effect. On the contrary, the correlation is weaker between the wind and the sea level over the Aegean Sea (Fig. 10c) in agreement with previous findings by Androulidakis et al. (2015) and Krestenitis et al. (2011); they showed that the Aegean Sea's storm surges are mainly determined by the SLP effect instead of wind, in contrast to the Adriatic Sea and northern Levantine Sea, where accompanying winds are the dominant factor of the sea-level variability. The wind–SLA correlation coefficients are relatively low and even negative in the Aegean Sea during September 2020 (< 0.4; Fig. 10c) in comparison with the Ionian Sea, where strong winds, especially during IANOS (> 0.6; Fig. 10d), enhanced the sea-level rise along the coasts. However, during the timespan of IANOS, the inverse barometer effect was also very strong over the Ionian Sea and the southwestern Aegean coasts ($R_{SLP} < -0.80$; Fig. 10b), especially during the storm landfall on 18/9 (Fig. 5k). A notable difference is also computed for the northwestern Crete, where the SLP affected the sea level, resulting in high negative R_P (< -0.80) during the IANOS passage (Fig. 10b). It is shown that although the storm surges over the Ionian Sea are mainly affected by the winds during typical storms, in the case of a Medicane coming from the central Mediterranean, the inverse barometer effect also contributed to the storm surge formation.

We further investigated the spatial variability of the wind direction impact on the affected coastline (Fig. 11). The highest correlation coefficients of both eastward and northward components (positive coefficients) during IANOS are computed for the central Ionian Sea, respectively (see Sect. 5.2). These winds were related to the eastward

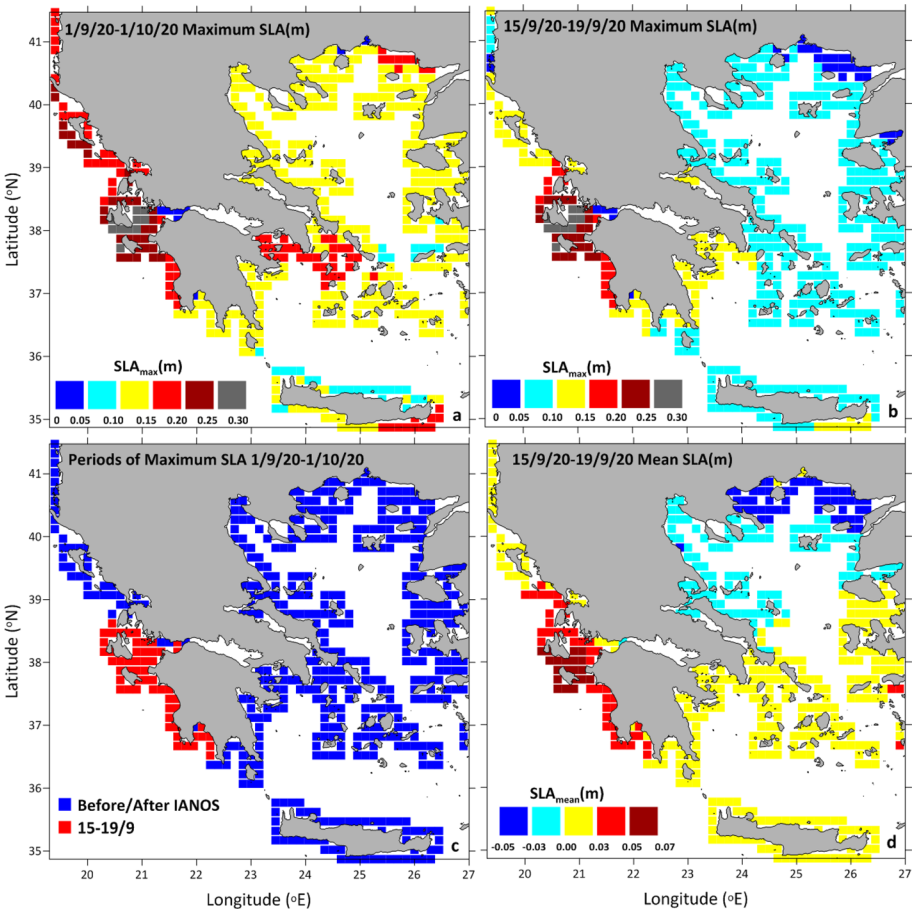

Fig. 9 Maximum sea-level anomaly (SLA_{max}; m) along the coastal cells of the Ionian and Aegean Seas during **a** September 2020 and **b** IANOS passage (15/9/20–19/9/20) derived from the HiReSS simulation. **c** Periods of SLA_{max} during (red) and before/after (blue) IANOS passage. **d** Mean SLA (SLA_{mean}) during IANOS passage (15/9/20–19/9/20)

propagation of IANOS and the accompanying onshore cyclonic winds (Fig. 4b), enhancing the accumulation of water masses near the coasts (Fig. 5k). The northern areas of Cephalonia and Lefkada islands were mainly affected by northerly winds (negative coefficients: < -0.4; Fig. 11b) as the storm propagated to the south after its landfall. Similarly, the eastward (Fig. 11a) and northward (Fig. 11b) winds were associated with the storm surges that occurred in the southern coasts of Peloponnesus ($R_P > 0.6$; Fig. 10d), related to the cyclonic currents that formed on 17/9 and 18/9 over the area. In the broader southwestern Aegean, southerly (positive coefficients in Fig. 11b) but easterly in this case (negative coefficients in Fig. 11a) winds influenced the storm surge variability; the correlation coefficient of the zonal wind component is higher than -0.8 over the eastern coasts of Cyclades archipelago and -0.6 along the western Aegean coasts (north of 38°N). The impact of the storm over the western Aegean, especially due to the surrounding cyclonic winds (southerlies and easterlies over this area), was visible on the sea elevation without though inducing

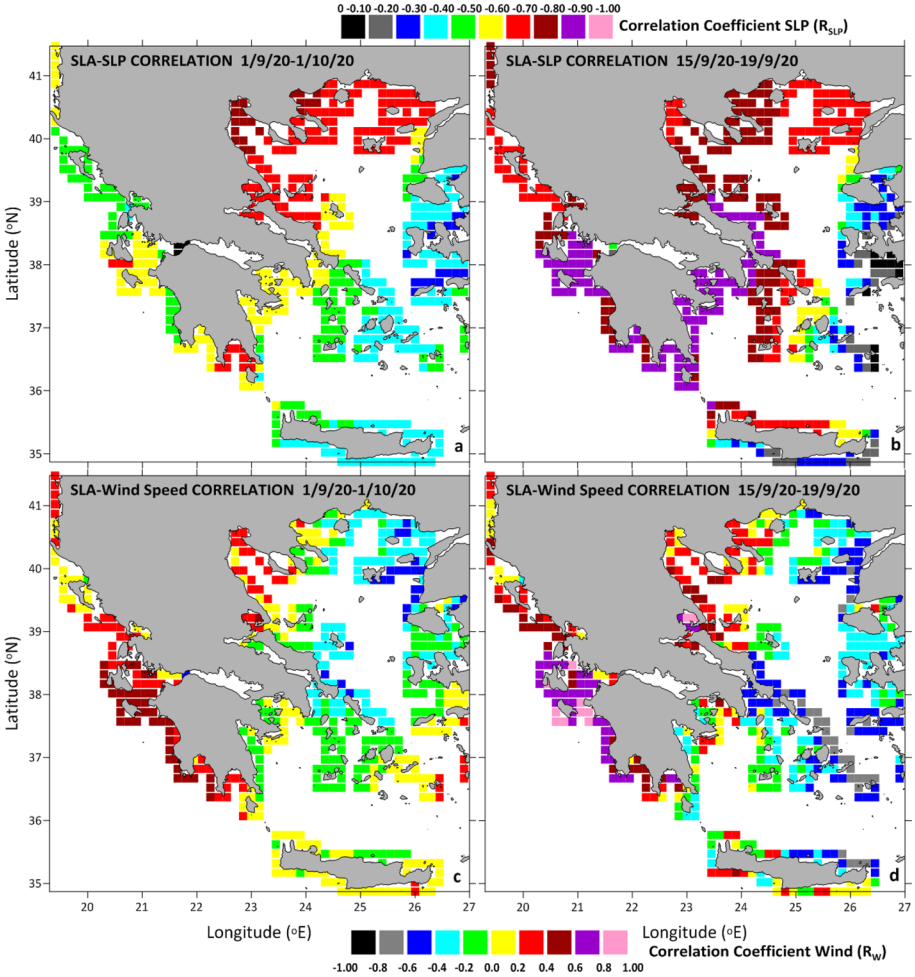

Fig. 10 Distribution of Pearson's correlation coefficients between the sea-level anomaly (SLA; HiReSS simulations) and the sea-level pressure (SLP; ECMWF forecasts) time series along the coastal cells of the Ionian and Aegean Seas during **a** September 2020 and **b** IANOS passage (15/9/20–19/9/20) derived from the HiReSS simulation. Respective correlation coefficients between SLA and wind speed timeseries during **c** September 2020 and **d** IANOS passage (15/9/20–19/9/20)

strong storm surges (Fig. 9b). The IANOS intrusion directly from the West, its landfall on the western Greek shores and then its southward propagation along the coast, altered the impact of the winds on sea-level elevation and thus the impact of storm surges on the coastal zone.

5.2 Coastal inundation

We showed that the largest storm surge levels have been detected over the central Ionian Sea, and especially at the southern islands and the neighboring coasts of the Greek mainland. Herein, the coastal inundation over these lowland coastal regions due to the IANOS

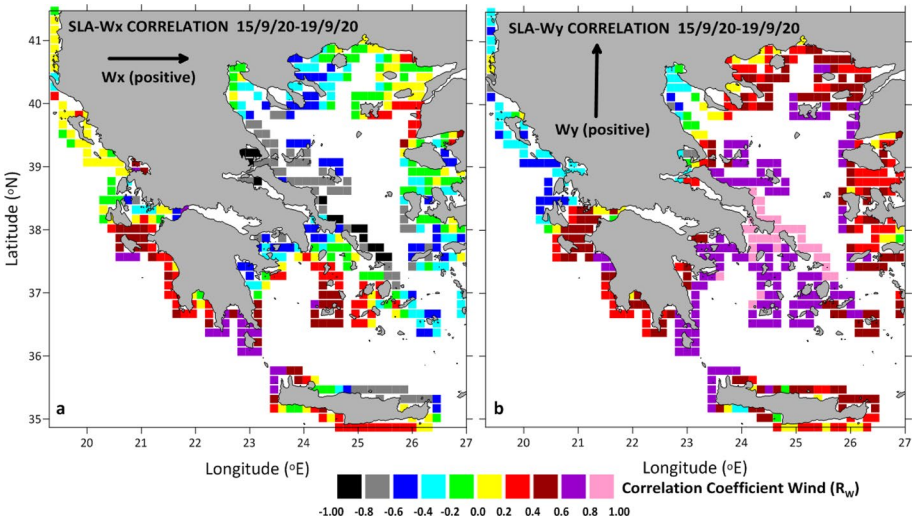

Fig. 11 Distribution of Pearson's correlation coefficients between the sea-level anomaly (SLA; HiReSS simulations) and the **a** zonal, **b** meridional wind components (ECMWF) along the coastal cells of the Ionian and Aegean Seas during the IANOS passage (15/9/20–19/9/20)

storm surges is estimated based on two techniques: satellite imagery (Sect. 5.2.1) and numerical simulations (Sect. 5.2.2).

5.2.1 Estimation of coastal inundation based on the NDWI

One of the main factors that determine the vulnerability of coastal regions, due to flooding under storm surge events, is the land elevation. DEM data (2 m resolution; see Sect. 2.2.2) are used to identify the areas of high flood risk. Eight coastal regions with extensive area of land elevation lower than 1 m have been identified based on the DEM data (Fig. 12a). These lowland areas were then classified with more detail (0.0–0.3 m, 0.3–0.6, 0.6–1.0 m; Figs. 13, 14 and Table 2). The highest storm surges, based on the SLA levels, ranged around 30 cm (see Sect. 5.1) in the broader coastal area of the central Ionian Sea inducing extended inundation phenomena, especially on 18/9 (see mass media photographic reports in Fig. 12b). The "flooded" and "wet" areas (for definitions see Appendix B) are computed based on the NDWI computation derived from two available Sentinel-2 images, before (15/9; Fig. 12c) and after (20/9; Fig. 12d) the storm surge. NDWI values larger than 0 represent cells covered by water (10 m resolution), while the negative values represent drier conditions of the land surface. A clear difference of the NDWI distribution is observed between the two dates; several areas with higher values (positive and closer to 1) were derived from the 20/9 satellite image (Fig. 12d). An example (Area 6: Livadi; Fig. 12a) is presented in Fig. 12e and f. It is noted that the satellite images during the storm passage over this area are not available and thus we cannot compute the precise inundation area exactly when the storm surge occurred (e.g., on 18/9). However, the computation of the NDWI from the first available image, 2 days after the storm surge (20/9), provides useful information about the coastal areas with increased moisture potentially related to the storm surge ("wet" areas) and more importantly about the remaining water ("flooded" areas).

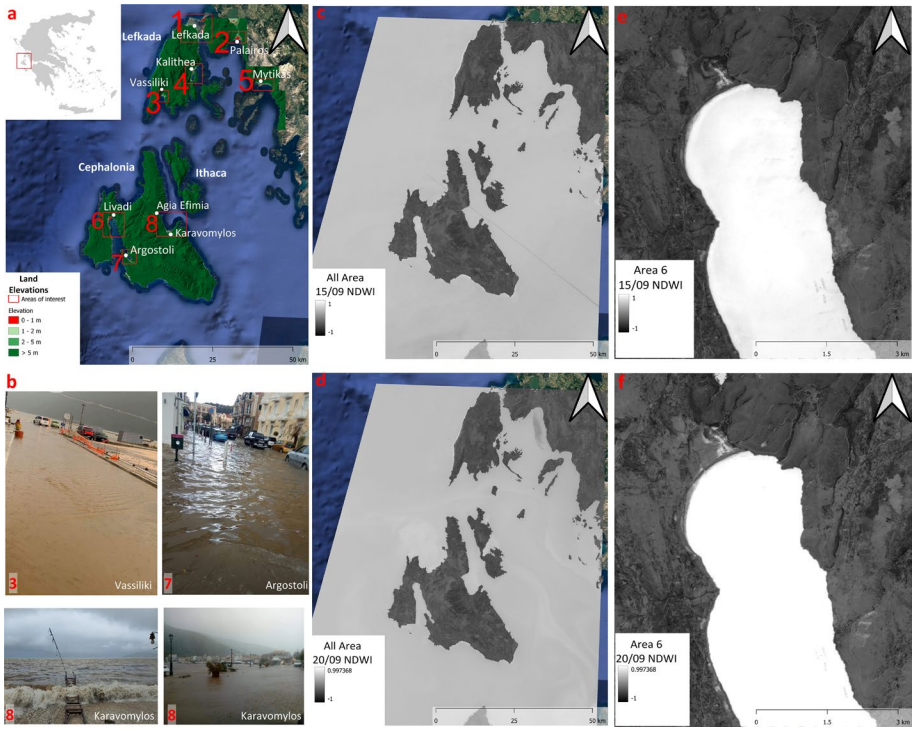

Fig. 12 **a** Land elevation derived from the high-resolution DEM (2-m spatial step) in the central Ionian Sea (inset map) laid over the respective Google Earth map. 8 characteristic coastal regions with extensive areas of lowland elevations (<5 m) are marked. **b** Mass media news' images showing four examples of storm surge flood impact during the IANOS Medicane at regions 3 (Lefkada island; https://aromalefkadas.gr/wp-content/uploads/2020/9/8743.jpg), 7 (Cephalonia island; https://www.protothema.gr/greece/article/1049137/kefalonia-plimmurise-i-paraliaki-tou-argostoliou/), and 8 (Cephalonia island; https://www.enikos.gr/society/ianos-kefalonia-eikones-katastrofis-ston-karavomylo-kai-tin-agia/1467506/) on 18/9. Distribution of the NDWI, derived from the available Sentinel-2 satellite images (c, e) before (15/9/20) and (d, f) after (20/9/20) the passage of IANOS over the south-central Ionian Sea (central panels) and a focused example over Area 6 (right panels). The full coverage of the satellite images is shown in panels (c) and (d)

The land elevation classification for each coastal region together with the respective "wet" and "flooded" areas due to the IANOS storm surges is presented in Figs. 13 and 14. The largest extent of the coastal zone with land elevation lower than 0.30 m is identified at Areas 1 (Fig. 13a) and 6 (Fig. 14c), where the potential area that is under the risk of inundation, if a 30-cm sea-level rise occurred, is around 1.1 km^2 and 0.6 km^2, respectively (Table 2). Most of the regions of the 0–30-cm class reveal positive mean NDWI differences (NDWI after the storm at 20/9 minus NDWI before the storm at 15/9) associated with the possible inundation processes that occurred during IANOS storm passage (Table 2). The largest mean NDWI difference among all areas was computed for Area 6 (0.10) at cells with land elevation between 0 and 0.3 m (Table 2). The high value of mean NDWI difference in Area 6 is associated with the large number of "wet" cells presented in Fig. 14d (light blue cells). The increased levels of NDWI after the storm are a strong indication that the IANOS-induced surge might have increased the moisture levels of the land. Moreover, a small portion of this area remained flooded on 20/9 (dark blue cells in Fig. 14d). The

Fig. 13 Maps of classified land elevation (DEM; left panels), flooded and wet areas as derived from the ▶ NDWI difference between 15/9 and 20/9 (right panels) for (a, b) Area 1, (c, d) Area 2, (e, f) Area 3, and (g, h) Area 4 shown in Fig. 12, respectively

area, still covered with water on 20/9, was around 2.7% of the lowland (0–0.3 m) coastal zone of the entire Area 6 (Table 2). A notable uncertainty of the method is related to other sources of increased moisture than flooding due to storm surges. The high moisture levels of the surface are associated not only with seawater intrusion from the nearby coast but also with intense precipitation rates and surface runoffs during the storm, especially regarding bilge-type study regions in the vicinity of intense sloping formations or drainage terrains (e.g., mountain and hill sides, thalwegs, etc.). In order to reduce this uncertainly, we focus on areas with land elevation below 0.30 m (storm surge level during IANOS) that are located close to the coastline. We also evaluate the littoral inundation patterns in Area 6 by simulating the flood intrusion of seawater over the same classified coastal zone (see Sect. 5.2.2).

The largest lowland stretch with remaining flooded cells on 20/9 was computed for Area 1 (0.06 km^2: 6.1% of the entire lowland (< 0.3 m) Area 1; Table 2; Fig. 13b). Flooded cells were detected over the northeastern and northwestern parts of Area 1, the Lefkada Lagoon, which is a region with extended erosion problems due to storm-induced waves and surges (Ghionis et al. 2015). The mean NDWI difference is 0.05 showing that although the remaining flooded expanse is larger than in Area 6, the storm surge effect during IANOS was smaller in Area 1. Area 2 also revealed high mean NDWI difference (0.07; Table 2) related to the large number of "wet" cells, especially at the central and west part of the coastal zone (Fig. 13d). Even though the flooded area is the highest among all regions (9.1%), the lowland elevation territory that can be potentially flooded is significantly smaller than in Areas 1 and 6 (Table 2; Fig. 14c), located at the central region, around 300 m away from the coast. The rest of the regions revealed smaller mean NDWI difference levels (Table 2) mainly due to the smaller extension of lowland areas (< 0.3 m), located mainly over narrow zones along the coasts. Very low NDWI differences (small number of "wet" cells) were computed for Areas 3, 4, and 5, where the lowland domain is also limited. Negative NDWI values and flood differences were even computed for Areas 7 and 8. Although strong inundation was observed at parts of the coastal zones (Fig. 12b), the urban infrastructure of these lowland regions (city of Argostoli in Area 7 and Agia Efimia-Karavomylos in Area 8) facilitated the quick retreat of flood waters and the drainage of remaining surface runoffs, reducing the performance of the NDWI to detect wet and flooded cells on 20/9. A second uncertainty of the approach is the lower accuracy in urban environments with organized stormwater drainage systems that facilitate the quicker removal of flood waters (McFeeters 2013). The uncertainty is higher when satellite images are not available exactly during the storm surge event (e.g., 18/9 in the case of IANOS over the central Ionian coasts) due to satellite absence over the study region or cloud contamination, which is common during atmospheric low-pressure systems.

5.2.2 Estimation of coastal inundation based on CoastFLOOD simulations

To tackle the aforementioned uncertainties, the CoastFLOOD model was implemented in both Bathtub (with and without hydraulic connectivity) and fully hydraulic flood routing approaches (see Sects. 2.1.3 and 2.1.4 and Appendix A). The numerical modeling of the coastal flooding due to the storm surge provides information of the inundation induced only

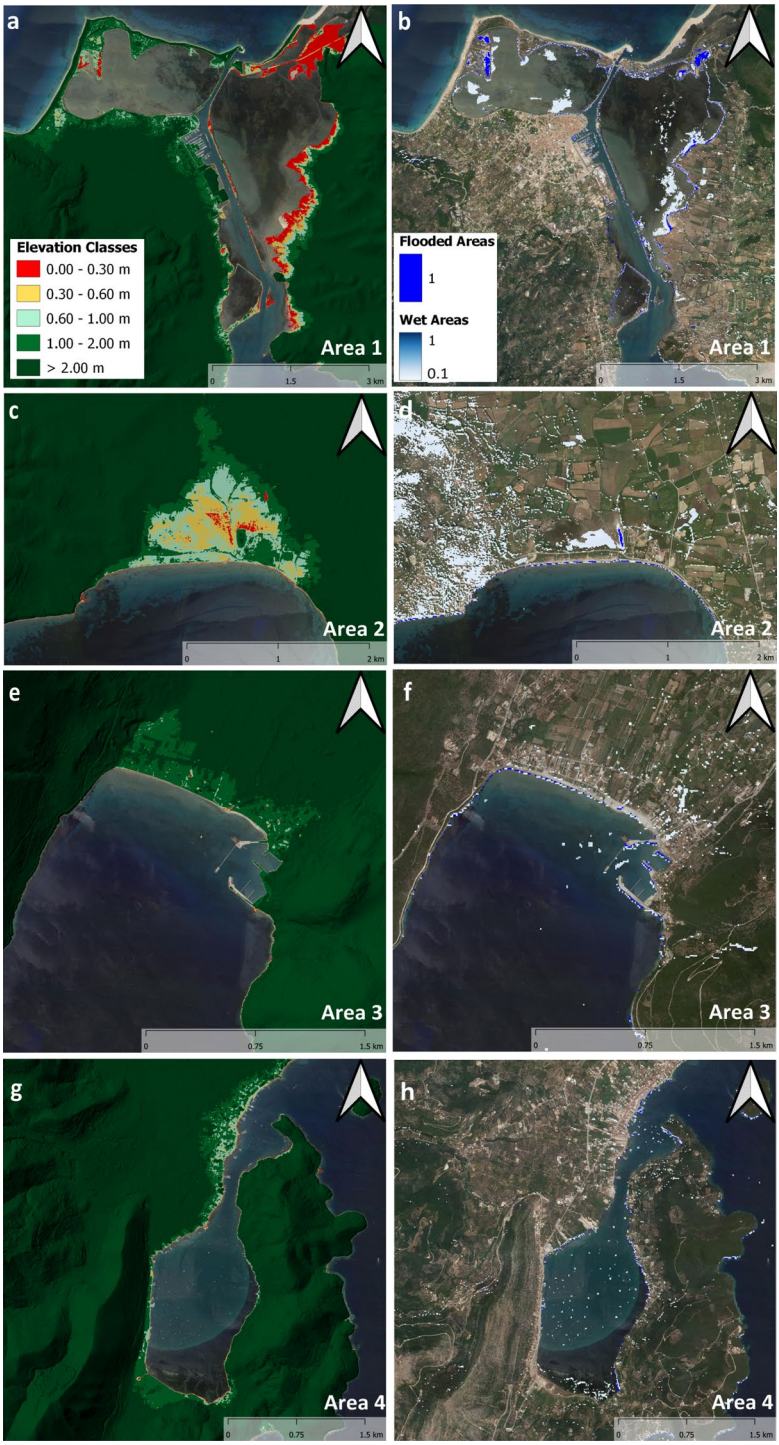
a
Elevation Classes
0.00 - 0.30 m
0.30 - 0.60 m
0.60 - 1.00 m
1.00 - 2.00 m
> 2.00 m
Area 1
b
Flooded Areas
1
Wet Areas
1
0.1
Area 1
c
Area 2
d
Area 2
e
Area 3
f
Area 3
g
Area 4
h
Area 4

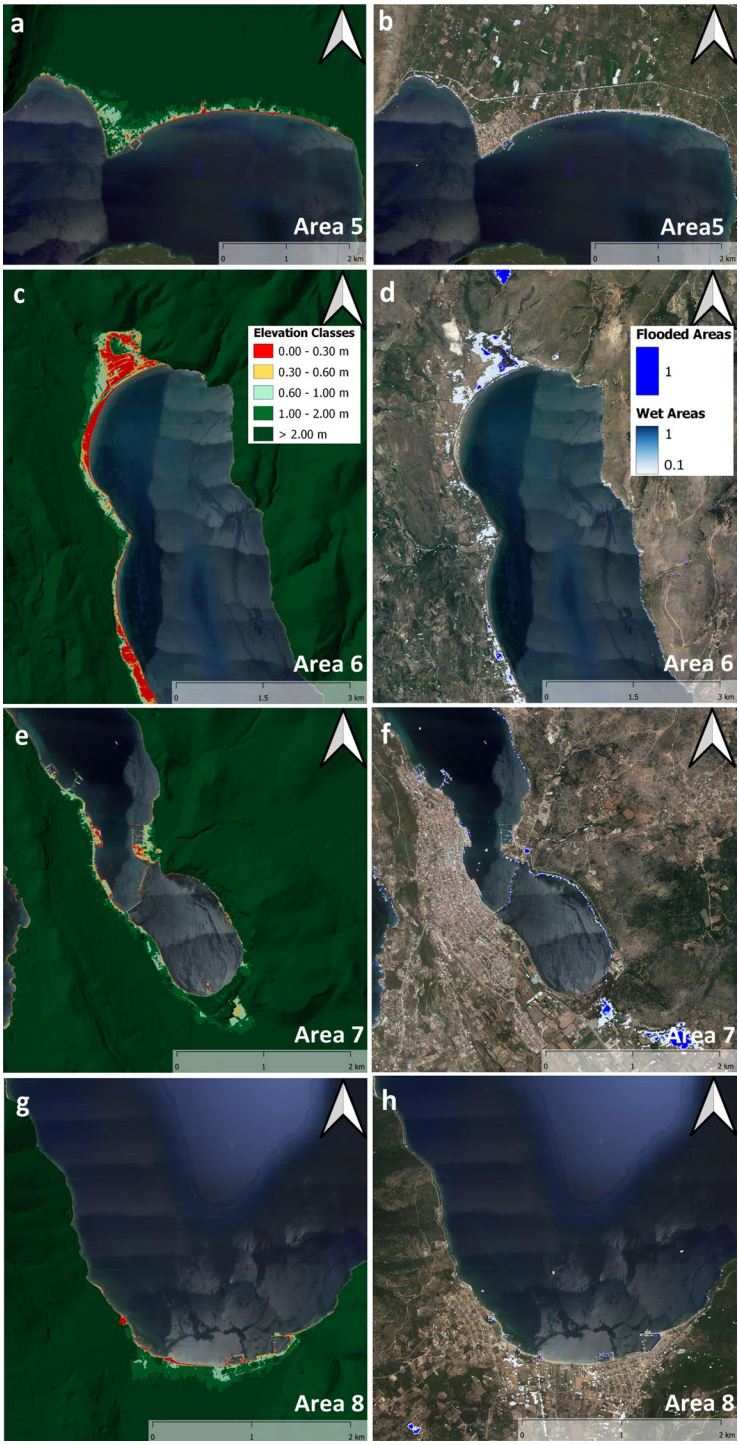

Fig. 14 Same as Fig. 13 for **a**, **b** Area 5, **c**, **d** Area 6, **e**, **f** Area 7, and **g**, **h** Area 8 shown in Fig. 12, respectively

Table 2 Features of flooded lowlands in Areas 1–8 of the study region: elevation class, total area (m^2), Normalized Difference Water Index (NDWI) mean difference, flooded areas (FA; m^2), coverage percentage of flood (%)

elevation class	Total area (m^2)	NDWI mean difference	FA (m^2)	Flood (%)	Elevation class	Total area (m^2)	NDWI mean difference	FA (m^2)	Flood (%)
Area 1					Area 5				
0–0.3 m	1,126,872	0.05022	68,264	6.1	0–0.3 m	73,596	0.03757	2,912	4.0
Area 2					Area 6				
0–0.3 m	45,484	0.07741	4,140	9.1	0–0.3 m	631,556	0.10490	17,168	2.7
Area 3					Area 7				
0–0.3 m	5,884	0.02765	192	3.3	0–0.3 m	44,500	−0.00559	−1,608	−3.6
Area 4					Area 8				
0–0.3 m	28,896	0.00506	−1,252	−4.3	0–0.3 m	41,036	−0.08010	−7,424	−18.1

by the storm surge (first uncertainty of the NDWI approach) and specifically during the IANOS storm passage and surge formation (second uncertainty of the NDWI approach). We focus on Area 6 (pilot case), which revealed the most extended coastal flooding among the study regions, based on the satellite-derived NDWI. Only steady-state inundation situations are considered herein, i.e., referring to an eventually constant sea-level boundary condition of storm surge maxima (SLA_{max}), derived from the hindcast simulation, for the timespan of storm-induced high seas on the coastline during the IANOS Medicane (Fig. 9b).

The accompanying barotropic currents over Area 6 increased during the storm surge (Fig. 15b), characterized by northward velocity components (Fig. 15d) due to the prevailing southeasterly winds caused by the storm. The wind speed started to increase in the morning of 17/9, a few hours before the passage of the low-pressure core over the study area (Fig. 15a); the lowest value of SLP occurred in the morning of 18/9 (SLP = 996.5 hPa). The increase in the wind speed gradually strengthened the storm-induced currents (Fig. 15b).

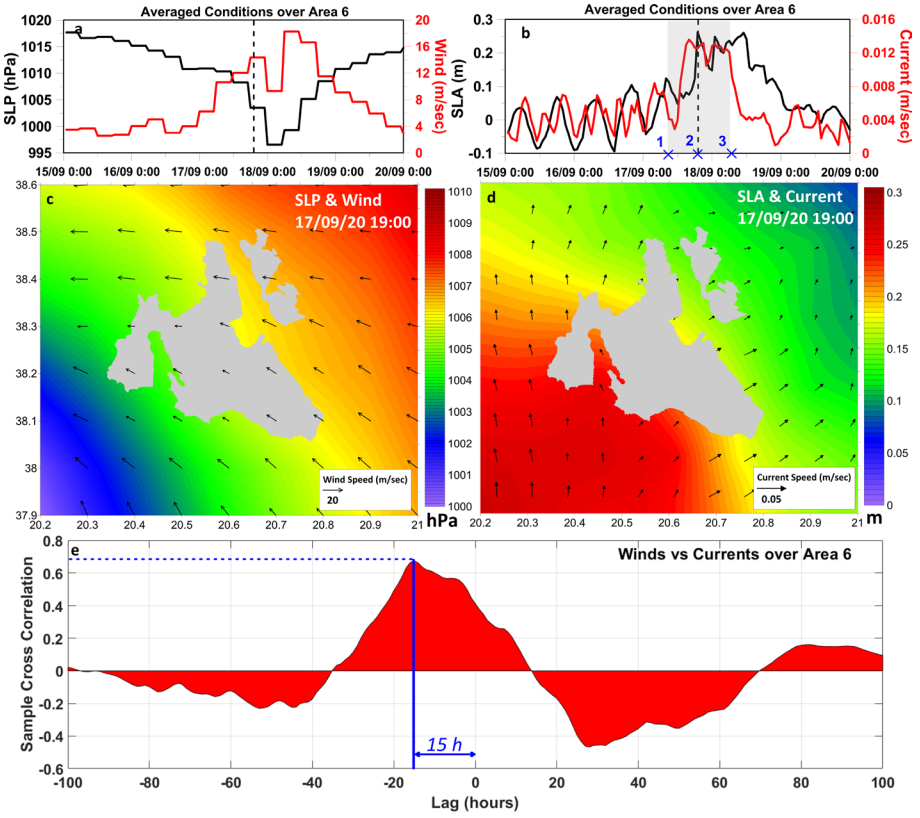

Fig. 15 Evolution of **a** sea-level pressure (SLP; hPa) and wind speed (m/sec), **b** sea-level anomaly (SLA; m) and current speed (m/sec) during 15/9–19/9 period, derived from the ECMWF-forced HiReSS hindcast simulation, averaged over Area 6 (Fig. 14d). Three characteristic dates of maximum SLA during the IANOS passage are also marked (with blue ×) on the x-axis. Maps of **c** SLP–winds and **d** SLA–currents over Cephalonia island on 17/9/20 19:00 (dashed line in panels a and b). **e** Cross-correlation between the wind and current speed showing the lag between the two parameters in hours (the blue lines mark the highest correlation coefficient)

The cross-correlation between the winds and currents, averaged over Area 6, was positive and relatively high at zero lag ($R_P = 0.41$; direct ocean response; Fig. 15e). However, the correlation coefficients increased with negative time lags showing a peak ($R_P = 0.70$) when the lag between the two parameters is approximately 15 h. This result confirms the lag of around 1/2 day between winds (Fig. 15a) and currents (Fig. 15b). The strongest storm surge occurred in the evening of 17/9 (0.262 m), few hours before the lowest SLP drop, due to accumulation of waters under the dominating southeasterly strong winds and the respective northward currents toward the inner gulf of Area 6, confirming the high correlation coefficients between southeasterly winds and SLA for the central Ionian islands (Fig. 11b). The storm surge boundary conditions, used in the CoastFLOOD simulations, were derived at three characteristic dates (Fig. 15b): (1) in the beginning of the storm surge ($SLA_{max1} = 0.124$ m on 17/9 08:00), (2) when the highest SLA peak occurred ($SLA_{max2} = 0.262$ m on 17/9 19:00), (3) when the SLA ranged over 0.2 m by the end of the storm surge ($SLA_{max3} = 0.237$ m on 18/9 06:00). Three additional threshold scenarios referring to the upper limits of theoretical SLA maxima, equal to $SLA_{max} = 0.3$, 0.6, and 1.0 m, were also considered. These are identified as extreme situations of sea-level rise in flood-prone areas presented mainly for comparison reasons.

The static Bathtub approach shows the potentially inundated lowland areas respective to SLA maxima (SLA_{max1}, SLA_{max2}, and SLA_{max3}) during the three storm surge levels (Fig. 15b). These areas represent the hypothetical scenario that all lowland areas with elevation below a specific threshold (SLA_{max} in this case) are flooded during the storm. The created maps (Fig. 16a) agree with the wet areas derived from the satellite NDWI analysis (Fig. 14d). Note that the total area with elevations below 0.3 m (Table 2) is equal to the potential inundated area presented in Table 3 (631,556 m^2). The flooded area extracted from the static Bathtub approach and $SLA_{max} = 0.262$ m (554,774 m^2) is slightly smaller than the scenario with $SLH_{max} = 0.3$ m (Table 3). In order to avoid overestimations of seawater flooded areas, as they may act as bilging reservoirs of surface water runoff, we included the hydraulic connectivity between raster grid cells with the use of the Bathtub HC approach (Fig. 16b) for the three identified storm surge phases (Fig. 15b). It is obvious that a detached, extensive, rural, inland area behind the coastal road that does not have any hydraulic connection with the coast is now excluded from the newly derived potential flood map for the three SLH_{max} thresholds (Fig. 16b). The estimated flooded area is about half of the theoretically computed region based on the static Bathtub approach for all cases (~47%; Table 3). Therefore, it is inferred that the excessive inland (agricultural) area, shown in Fig. 16a (eradicated in Fig. 16b), may serve as drainage reservoir and can be flooded with water originated from sources different than the coastal storm surge (e.g., rainwater from local intense precipitation and stormwater surface runoff from the surrounding higher grounds). The only case that exceeds the 50% of the threshold area is related to the scenario with storm surge up to $SLA_{max} = 1$ m (Table 3); in this hypothetical event, 70% of the coastal area with elevation below 1 m might be inundated with seawater due to an extreme sea-level rise event (1 m). Inland-extended inundated areas were also detected in the southwestern part of the coastal region, where storm surge impact was visible onshore around 200 m from the coastline.

A more conservative yet realistic approach, using the full hydraulic version of the CoastFLOOD inundation model (see Sect. 2.1.3 and Appendix B), is presented in Fig. 16c for the three simulated storm surge boundary conditions of IANOS and in Fig. 16d for three extreme theoretical scenarios of 0.3, 0.6, and 1 m. The northern part of the gulf showed similar results to the Bathtub HC approach, where the surge-induced flood extended over a long but narrow zone along the coast. The parts of the southwestern coastal zone that

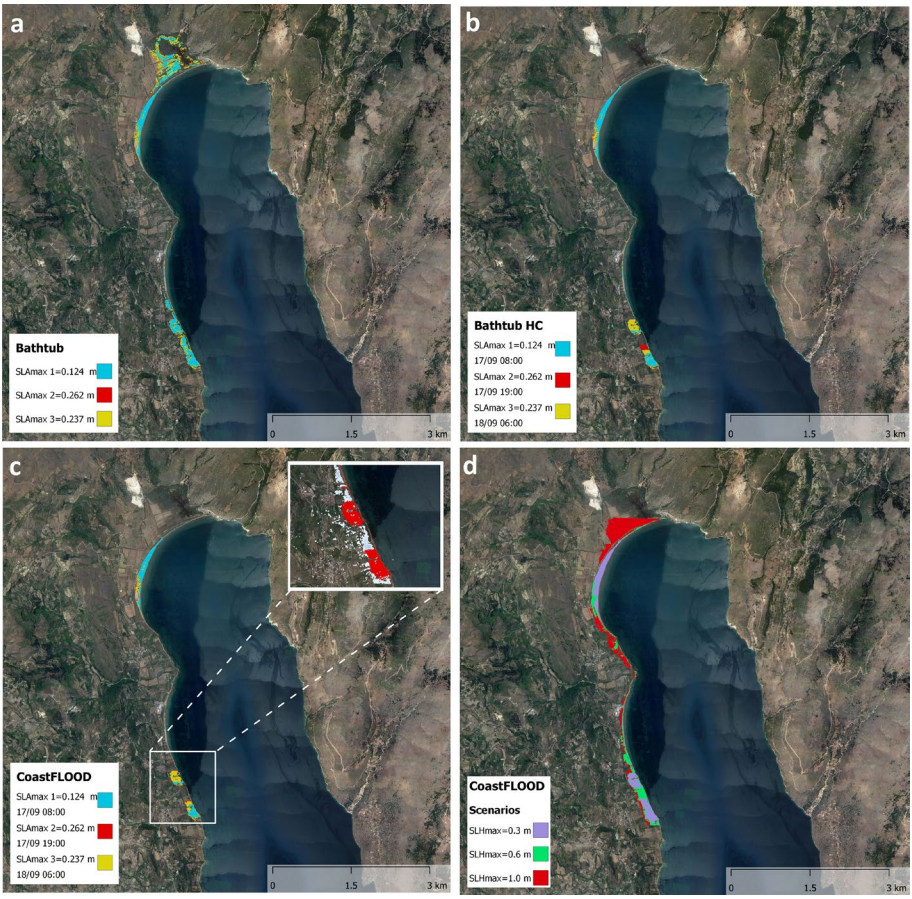

Fig. 16 Maps of flooded areas derived from three modeling approaches: **a** simple Bathtub, **b** Bathtub with hydraulic connectivity (HC), and c CoastFLOOD with realistically simulated storm surges during three characteristic dates ($SLA_{max1}=0.124$ m, $SLA_{max2}=0.262$ m, $SLA_{max3}=0.237$ m) of IANOS passage over Area 6 (Fig. 14d). **d** Potential flooded area derived from CoastFLOOD simulations based on three extreme scenarios of storm surge (0.3, 0.6, 1.0 m). An example comparing the estimations between CoastFLOOD (model; $SLH_{max}=0.262$ with red) and NDWI (satellite; wet areas with light blue) over the southwestern coastal region is presented in the inset of panel c. Note that patches formulated by cells corresponding to higher SLA_{max} values (e.g., of yellow, green, and red colors) are overlaid with the respective cell patches corresponding to lower SLA_{max} values (e.g., of light blue or purple color)

were computed as flooded with Bathtub HC are fewer in this case; the storm-induced run-up of seawater was also significant in these specific parts of the coastal zone (~200 m; Fig. 16c), in agreement with the "wet" areas derived from the satellite imagery (inset in Fig. 16c). The flood area gradually expands under the three more extreme scenarios with $SLH_{max} \geq 0.3$. The largest inundated area was computed in the case with SLA of 1 m, where surge-originated waters might cover a large part of the coastal zone (66% of the area derived by the static Bathtub approach; Table 3) with strong inland overflow (Fig. 16d). Especially in the northern part of the gulf, the waters might inundate hinterland areas, located at more than 400 m from the coastline.

Table 3 Features of estimated total flooded areas (FA; m^2), by numerical simulations with CoastFLOOD model in: (a) static Bathtub approach, (b) Bathtub approach with hydraulic connectivity (HC), and (c) CoastFLOOD hydraulic inundation approach, in Area 6

Cases	Total flooded area, FA (m^2)		
SLA_{max} (m)	(a) Static Bathtub FA (m^2)	b) Bathtub HC FA (m^2)	(c) CoastFLOOD hydraulic inundation FA (m^2)
	SLA maxima by realistic storm surges		
0.124	342,172	163,784	123,060
0.237	516,676	247,532	204,372
0.262	554,712	261,580	218,400
	SLA maxima by threshold scenarios		
0.3	631,556	315,680	253,924
0.6	975,740	493,604	442,708
1.0	1,355,396	973,556	902,544

Cases refer to $SLA_{max} = 0.124$ m, 0.237 m, 0.262 m (realistic storm surges), 0.3 m, 0.6 m, and 1 m (threshold scenarios of maximum sea-level rise in the study area)

6 Summary and discussion

The IANOS low-pressure system was one the most severe storms that formed in the Mediterranean Sea with Category 2 Hurricane characteristics (Lagouvardos et al. 2021). IANOS induced significant storm surges along its pathway and increased the sea level over the central Ionian Sea, specifically in the Ionian Islands and in the neighboring western Greek coasts. The operational forecast system Wave4us (http://wave4us.web.auth.gr; Krestenitis et al. 2017) based on the HiReSS storm surge model predicted the sea-level increases during the formation and evolution of IANOS in real-time. In order to study the storm surge variability along the affected coastal areas, we additionally conducted a hindcast numerical simulation during August–September 2020, based on the same setup as the forecast mode of the HiReSS model but forced with the higher-resolution ECMWF atmospheric fields. The comparison of the model results against available tide-gauge observations, confirmed the ability of the model to efficiently reproduce the prevailing barotropic circulation during the IANOS Medicane. Our results showed that the performance of the hydrodynamic numerical forecasts is strongly related to the efficiency and spatial resolution of the real-time meteorological predictions, especially during severe meteorological events that are difficult to predict with high accuracy in real-time (intensity and track calculation). We analyzed the characteristics of the storm surges and estimated the coastal inundation levels using fields derived from the hindcast numerical simulation.

The northward propagation of IANOS from the vicinity of the northern African coast (Gulf of Sidra) toward the Ionian Sea formed a moving cyclonic eddy with relatively strong anticlockwise currents following the track of the storm, increasing the sea-level anomaly (SLA), mostly below the core of the system in the open sea. The eastward turn of IANOS and the approach of Ionian Islands and coasts induced significant storm surges and onshore currents that caused inundation at several coastal areas. The cyclonic currents due to the IANOS passage over the Ionian Sea controlled the barotropic circulation in the entire Adriatic Sea (northwestward currents) increasing the SLA on 17/9. Toomey et al. (2022) showed that Medicane-induced winds from the southeast may generate extreme total water

levels in the northern Adriatic in a similar way to the prevailing Sirocco-induced circulation, which is usually responsible for storm surges in the region. The coverage area of the storm-induced eddy showed the highest extents simultaneously with the SLA peaks in the afternoon of 17/9, covering the entire region between south Italy and western Greece. A clear cyclonic (south of the storm)–anticyclonic (north of the storm) eddy dipole was formed during the evolution of the Medicane from its formation in the Gulf of Sidra to the landfall on western Greek continental land. The vorticity distribution showed that the prevailing cyclonic currents, especially during 17–18/9, affected the coastal circulation before (17/9) and during (18/9) the landfall of the storm and started raising the sea level at several coastal areas prior to the arrival of the storm's core. The prolonged stall of the Medicane over the central Ionian on 18/9 induced cyclonic onshore winds and respective currents along the southern Ionian, increasing the storm surge levels along the coasts. The highest storm surge reached the level of 30 cm at several coastal areas of the Ionian Sea, mainly around Cephalonia Island a few hours before the IANOS landfall. The topographic peculiarities of the coastal zone in combination with the onshore wind/currents had also increased the coastal SLA in specific areas a few hours before the landfall of the Medicane's eye (e.g., on the evening of 17/9). Previous studies showed that during typical Mediterranean storms, the surges over the Adriatic and Ionian Sea are mainly determined by the strong accompanying winds, while the inverse barometer effect is the main contributor on the storm surge formation in the Aegean Sea (Krestenitis et al. 2011; Androulidakis et al. 2015; Makris et al. 2016). In the case of IANOS, where a Medicane intruded over the Ionian Sea directly from the West and remained over the central coasts for several hours, both wind and barometric pressure effects contributed to the sea-level increases.

Several coastal areas of the central Ionian Sea with land elevation lower than 30 cm have been flooded due to the IANOS storm surge. Ocean color images before and after the event were used to compute the Normalized Difference Water Index (NDWI) and provided an estimation for the extent of inundation during the storm and the remaining flooded areas after it. However, the absence of available images during the storm and the unknown contribution of other sources to the estimated flood creates uncertainty about the exact area of inundation coverage due to the storm surge. We isolated the storm surge contribution on the flooding levels of the coastal areas with the use of an inundation model that includes the realistic storm surge levels, derived from the ocean simulations, as boundary conditions along the coast. The model simulated the flooding processes that are related to the storm surge, excluding thus other potential sources. Our results showed that although the simulated flooded area is significantly smaller than the satellite-derived estimation, a large part of the study area's coastal zone was covered with seawaters during the peak of the storm surge, revealing in some cases wave run-up that extended 200 m inland. It is noted that even though the model-derived flooded areas are smaller than the initial estimation, they are located inside the regions characterized as "wet," based on the NDWI technique. The combination of the two techniques, especially if satellite images are available during a storm, together with high-resolution land elevation data and realistic storm surge information along the coast, can provide an efficient description of the coastal inundation associated with a severe storm surge event, especially in remotely accessed places or in places without any monitoring (Ogashawara et al. 2013).

The wave-induced coastal flooding is not considered in this paper. The wave run-up on the coast can cause overtopping or breaching of physical defenses (dunes) or engineered structures (dikes, revetments, breakwaters, etc.). This, potentially catastrophic, influence is usually confined in a rather limited area a few (tens of) meters inland from the shoreline, depending on the magnitude of the incident wave period, thus being out of scope for the present paper.

Furthermore, since there was no special reporting on hazardous swells and severe wave attack during the IANOS event, only a noticeable sea-level increase, we herein focused only on the storm surge impact at the coast that can drive extended floods, covering large lowland areas and reaching a few hundreds of meters inland form the coastline. Nevertheless, the compound flooding processes (i.e., combined inundation due to seawater uprush and rainwater runoff by concurrent heavy precipitation and high storm surges; Wahl et al. 2015; Bevacqua et al. 2019; Hendry et al. 2019; Gori et al. 2020) are also not considered in this paper, as there is no available operational modeling platform for (watershed and stream) catchments flooding by surface runoffs in the study area. These are set as future goals of research.

7 Concluding remarks

An integrated approach based on hydrodynamic ocean simulations coupled to meteorological and coastal flooding simulations *in tandem* with field and satellite observations was used to analyze the marine weather conditions, the storm surge characteristics, and the coastal inundation processes due to the impact of IANOS Medicane in September 2020. The improvement in atmospheric forcing increases the efficiency of the ocean predictions and thus the quality of the storm surge estimations. The coupled numerical methodology provides short-term and real-time predictions of the flooding status on a coastal scale, useful to the associated local authorities and first responders during an extreme meteorological event. The added value of the study is the presentation and evaluation of a comprehensive methodology that can be applied in several extreme events near coastal areas and is thus valuable for broader use, especially in the context of increasing extreme events under climate change, with pronounced coastal impacts.

Both wind and atmospheric pressure levels affected the storm surge variability over the Ionian Sea, which is usually controlled by the wind conditions in the case of a typical Mediterranean storm (without tropical characteristics). The direct intrusion of a Medicane from the central Mediterranean toward the Ionian Sea, followed by a cold wake similar to tropical storms, may form storm surges over the coastal areas even before the storm's landfall, due to the accompanying cyclonic winds and onshore currents. Medicanes affect the coastal areas and form intense storm surges with two ways: either by the accumulation of waters due to onshore wind/currents before the landfall of the storm's eye, or by the direct impact of the inverse barometer effect over the coast. Storm surges in the order of 30 cm caused extensive flooding over lowland coastal areas during IANOS Medicane, as confirmed by both satellite and numerical data. The hydraulic connectivity between the lowland areas determined the spatial extents of inundation during the storm surge. Coastal flood modeling can mitigate some of the satellite data-based NDWI limitations, but can also be guided by NDWI findings (e.g., as to the most extended region of coastal flooding). The flooding simulations, based on different storm surge scenarios, including future climatic projections, can improve the design of appropriate protection infrastructure over coastal lowland regions, mitigating their vulnerability against storm surge risks.

Appendix A

CoastFLOOD is a 2-D horizontal, mass balance, coastal inundation model, which is based on the concepts of the established LISFLOOD-FP model for coastal (and river) plain flooding (Bates et al. 2005, 2010; Hunter et al. 2005). The robustness of LISFLOOD-FP model's approach has been thoroughly validated and broadly applied in floodplain areas (Horritt and Bates 2002; Neal et al. 2011; Seenath et al. 2016). We hereby combine this approach with a wet/dry cell assignment technique for flood fronts over steep slopes (Brufau et al 2004; Castro et al. 2005). Therefore, the model considers the wetting and drying of separate cells in the integration process, yet all computations are set to finish when the highest flooded area is achieved, viz. it is not allowed to simulate the retreat of seawater toward the sea after the storm surge starts to attenuate on the coastal boundary. The flood routing module makes use of very fine spatial resolution ($dx = 2$ m; see Sect. 2.2) computational domains based on raster grids (Horritt and Bates 2001).

CoastFLOOD has a rather simplistic finite difference hydraulic flow module of very high resolution, based on a raster grid, particularly fitted to reproduce the 2-D water expansion due to surge-induced seawater setup causing coastal inundation (Bates and De Roo 2000; Horritt and Bates 2001; Makris et al. 2020; Skoulikaris et al. 2021). A meridional-to-zonal direction decomposition of the inundation flow components allows the 1-D flow equations for seawater overland propagation to be solved separately for each front of a typical 2-D raster grid cell (Bates et al. 2005; Bradbrook et al. 2004; Hunter et al. 2005). This provides an easy 2-D solution representation in each horizontal direction (zonal and meridional, i.e., x- and y-direction, respectively) and final integration of the flow (Bates et al. 2010). The continuity equation corresponds to the mass conservation principle for the calculation of local water depth (free-surface height) in each gridded cell (Bates et al. 2005). The flood flow route is then estimated by a simplistic quad-tree search algorithm for downstream cells and saved in an updated matrix every time step by a dry/wet cell storage code, based on the difference of hydraulic head between neighboring cells (Hunter et al. 2006). The flow rate in each cell and direction are derived from a Manning's law approach using the water surface elevation above land level incorporating bottom friction. The continuity and momentum equations for the calculation of change in the volume of flow, following Neal et al. (2011), are described in detail by Skoulikaris et al. (2021).

CoastFLOOD model also incorporates a "static-level" inundation module operating in "Bathtub" mode, i.e., tracing and marking the flood-prone lowland cells with ground elevation z below a predefined threshold (e.g., the storm surge water level) on the computational raster grid (Didier et al. 2019; Schmid et al. 2014; Yin et al. 2017). The Bathtub technique is too simplistic in terms of hydraulic processes and may lead to non-physical overestimations of coastal flood extents (Didier et al. 2015; Ramirez et al. 2016; Vousdoukas et al. 2016). Thus, an enhanced bathtub approach with hydraulic connectivity ("Bathtub HC" mode), i.e., allowed water flow in adjacent cardinal and diagonal directions ("eight-side rule"), is also available to constrict implausible overestimation of possibly inundated areas by coastal seawater masses (Karamouz and Fereshtehpour 2019; West et al. 2018; Williams and Lück-Vogel 2020). This method neglects bottom friction due to floodplain terrain roughness and permeability, time integration for the entire duration of the storm surge event, and water flow height and velocity that affect the overland flood extension from the coastline. However, it performs better than a mere bathtub approach and therefore provides more conservative inundation results with less unrealistically detached flooded areas.

The potentially flooded coastal land area is precalculated, as the hydraulic-connectivity bathtub module runs in CoastFLOOD's initial phase of simulation before it commences the full-scale numerical solution by the spatial- and time-stepping algorithm (Bates and De Roo 2000; Bates et al. 2005, 2010; Skoulikaris et al. 2021). This eventually helps with deriving the coverage percentage of inundated areas (by number of wet cells) that are numerically estimated by the flood flow model compared to the potentially flooded areas of the raster grid (Makris et al. 2020; Skoulikaris et al. 2021). Typically, inconsistencies in the digital elevation model (DEM) may induce inaccuracies in the derivation of flooded areas. In the present case study, the implemented grid is of very high resolution ($dx = 2$ m), taking into account the most significant topographic details in the coastal zone, such as engineered urban infrastructure, buildings, ports, roads, and natural formations in the floodplain, farmlands, beach slopes, dunes, emerged barriers, hillocks, rural geodetic peculiarities (Murdukhayeva et al. 2013; Kahl et al. 2022).

Appendix B

The Normalized Difference Water Index (NDWI) is computed based on Sentinel-2 Band3 and Band8 bands of the ocean color images:

$$NDWI = \frac{\text{Band3} - \text{Band8}}{\text{Band3} + \text{Band8}} \tag{1}$$

where Band3 and Band8 are the visible green light and the near-infrared radiation of the spectrum, respectively. The estimation of the coastal flooded area is based on the derived NDWIs of two images, the one before (15 September) and the second after (20 September) the IANOS passage; the difference of the two NDWIs provides information about the inundated area. Specifically, after calculating NDWI for each of the two images, the magnitude of the difference in NDWI for each 10-m pixel (NDWI value after the storm minus the NDWI value before the storm) was calculated. A positive difference is interpreted as an increase in soil moisture due to the storm indicating a prior presence of water on that pixel. In order to conservatively identify the areas that received large amounts of water due to the storm, it is considered that pixels with difference values greater than 0.1 correspond to wet soil ("wet" areas that were potentially flooded during the storm). The next step was to filter the NDWI values calculated for 15 and 20 September with a threshold of zero (all cells with positive NDWI values are identified as cells full of water) and by this to identify the actual water areas before and after the storm. The difference between the two corresponds to the areas that were still flooded on 20 September due to the storm ("flooded" areas). It is worth pointing out that the areas identified as flooded due to the storm had increased NDWI difference values greater than 0.5 in several cases, which confirms the result. It is noted that although the method is not able to distinguish the source of the flood (e.g., storm surge, drainage runoff, precipitation), it provides useful information about the inundation levels of lowland areas close to the coastline.

Acknowledgements Parts of this research were co-financed by the European Union and Greek national funds through the Operational Program "Competitiveness, Entrepreneurship and Innovation," under the call "RESEARCH–CREATE–INNOVATE"; project name: ACCU-WAVES; project code: T1EDK-05111. The original configuration of HiReSS model's sea-level operational forecasts was developed within the WaveForUs project, funded by the national action "COOPERATION 2011: Partnerships of Production and Research Institutions in Focused Research and Technology Sectors" in the framework of the operational program "Competitiveness and Entrepreneurship (NSRF2007-2013)."

Funding This study was funded by RESEARCH–CREATE–INNOVATE"; project name: ACCU-WAVES, project code T1EDK-05111.

Declarations

Conflict of interest The authors have not disclosed any conflict of interest.

References

Androulidakis YS, Krestenitis YN (2022) Sea surface temperature variability and marine heat waves over the Aegean, Ionian, and Cretan Seas from 2008–2021. J Mar Sci Eng 10(1):42

Androulidakis YS, Kombiadou KD, Makris CV, Baltikas VN, Krestenitis YN (2015) Storm surges in the Mediterranean Sea: variability and trends under future climatic conditions. Dyn Atmos Oceans 71:56–82

Anggraini N, Marpaung S, Hartuti M (2018) Ujung pangkah shoreline change analysis using edge detection method and normalized difference water index. J Penginderaan Jauh dan Pengolah Data Citra Digit 14(2)

Bakkensen LA (2017) Mediterranean hurricanes and associated damage estimates. J Extrem Events 4(02):1750008

Ballesteros C, Jiménez JA, Viavattene C (2018) A multi-component flood risk assessment in the Maresme coast (NW Mediterranean). Nat Hazards 90(1):265–292

Barnard PL, van Ormondt M, Erikson LH, Eshleman J, Hapke C, Ruggiero P, Adams PN, Foxgrover AC (2014) Development of the coastal storm modeling system (CoSMoS) for predicting the impact of storms on high-energy, active-margin coasts. Nat Hazards 74(2):1095–1125

Bates PD, De Roo APJ (2000) A simple raster-based model for flood inundation simulation. J Hydrol 236:54–77

Bates PD, Dawson RJ, Hall JW, Horritt MS, Nicholls RJ, Wicks J, Hassan M (2005) Simplified two-dimensional numerical modelling of coastal flooding and example applications. Coast Eng 52(9):793–810

Bates PD, Horritt MS, Fewtrell TJ (2010) A simple inertial formulation of the shallow water equations for efficient two-dimensional flood inundation modelling. J Hydrol 387(1–2):33–45

Bevacqua E, Maraun D, Vousdoukas MI, Voukouvalas E, Vrac M, Mentaschi L, Widmann M (2019) Higher probability of compound flooding from precipitation and storm surge in Europe under anthropogenic climate change. Sci Adv 5(9):p.eaaw5531

Bradbrook KF, Lane SN, Waller SG, Bates PD (2004) Two-dimensional diffusion wave modelling of flood inundation using a simplified channel representation. Int J River Basin Manag 2:211–223

Brufau P, García-Navarro P, Vázquez-Cendón ME (2004) Zero mass error using unsteady wetting–drying conditions in shallow flows over dry irregular topography. Int J Num Meth Fluids 45(10):1047–1082

Castro MJ, Ferreiro AF, García-Rodríguez JA, González-Vida JM, Macías J, Parés C, Vázquez-Cendón ME (2005) The numerical treatment of wet/dry fronts in shallow flows: application to one-layer and two-layer systems. Math Comp Mod 42(3–4):419–439

Cavicchia L, von Storch H, Gualdi S (2014) Mediterranean tropical-like cyclones in present and future climate. J Clim 27(19):7493–7501

Chrisafinos D, Kavvadas I (2016) Quality assessment of the new backgrounds LSO25. In: 14th National conference on chartography of the greek scientific association of chartography, titled "The chartography in a changing world", 2–4 November 2016 (in Greek)

Cid A, Menéndez M, Castanedo S, Abascal AJ, Méndez FJ, Medina R (2016) Long-term changes in the frequency, intensity and duration of extreme storm surge events in southern Europe. Clim Dyn 46(5):1503–1516

Cioni G, Cerrai D, Klocke D (2018) Investigating the predictability of a Mediterranean tropical-like cyclone using a storm-resolving model. Q J R Meteorol Soc 144:1598–1610. https://doi.org/10.1002/qj.3322

Colle BA, Buonaiuto F, Bowman MJ, Wilson RE, Flood R, Hunter R, Mintz A, Hill D (2008) New York City's vulnerability to coastal flooding: storm surge modeling of past cyclones. Bull Am Meteor Soc 89(6):829–842

Dafis S, Claud C, Kotroni V, Lagouvardos K, Rysman JF (2020) Insights into the convective evolution of Mediterranean tropical-like cyclones. Q J R Meteorol Soc 146(733):4147–4169

Darmaraki S, Somot S, Sevault F, Nabat P (2019) Past variability of Mediterranean Sea marine heatwaves. Geophys Res Lett 46(16):9813–9823

de Vries H, Breton M, de Mulder T, Krestenitis Y, Proctor R, Ruddick K, Salomon JC, Voorrips A (1995) A comparison of 2D storm surge models applied to three shallow European seas. Environ Softw 10(1):23–42

Didier D, Bernatchez P, Boucher-Brossard G, Lambert A, Fraser C, Barnett R, Van-Wierts S (2015) Coastal flood assessment based on field debris measurements and wave runup empirical model. J Mar Sci Eng 3(3):560–590

Didier D, Baudry J, Bernatchez P, Dumont D, Sadegh M, Bismuth E, Bandet M, Dugas S, Sévigny C (2019) Multihazard simulation for coastal flood mapping: Bathtub versus numerical modelling in an open estuary, Eastern Canada. J Flood Risk Manag 12:e12505

Emanuel K (2005) Increasing destructiveness of tropical cyclones over the past 30 years. Nature 436(7051):686–688

Flaounas E, Davolio S, Raveh-Rubin S, Pantillon F, Miglietta MM, Gaertner MA, Hatzaki M, Homar V, Khodayar S, Korres G, Kotroni V (2021) Mediterranean cyclones: current knowledge and open questions on dynamics, prediction, climatology and impacts. Weather and climate dynamics discussions, pp 1–68

Fortelli A, Fedele A, De Natale G, Matano F, Sacchi M, Troise C, Somma R (2021) Analysis of sea storm events in the Mediterranean Sea: the case study of 28 December 2020 sea storm in the Gulf of Naples, Italy. Appl Sci 11:11460

Gao BC (1996) NDWI—a normalized difference water index for remote sensing of vegetation liquid water from space. Remote Sens Environ 58(3):257–266

Ghionis G, Poulos SE, Verykiou E, Karditsa A, Alexandrakis G, Andris P (2015) The impact of an extreme storm event on the barrier beach of the Lefkada lagoon, NE Ionian Sea (Greece). Mediterr Mar Sci 16(3):562–572

Gori A, Lin N, Smith J (2020) Assessing compound flooding from landfalling tropical cyclones on the North Carolina coast. Water Resour Res 56(4):e2019WR026788

Hendry A, Haigh ID, Nicholls RJ, Winter H, Neal R, Wahl T, Joly-Laugel A, Darby SE (2019) Assessing the characteristics and drivers of compound flooding events around the UK coast. Hydrol Earth Syst Sci 23(7):3117–3139

Horritt MS, Bates PD (2001) Predicting floodplain inundation: raster-base modelling versus the finite-element approach. Hydrol Process 15:825–842

Horritt MS, Bates PD (2002) Evaluation of 1D and 2D numerical models for predicting river flood inundation. J Hydrol 268:87–99

Hunter NM, Horritt MS, Bates PD, Wilson MD, Werner MG (2005) An adaptive time step solution for raster-based storage cell modelling of floodplain inundation. Adv Water Resour 28(9):975–991

Hunter NM, Bates PD, Horritt MS, Wilson MD (2006) Improved simulation of flood flows using storage cell models. Proc Inst Civ Eng Water Manag 159:9–18

Kahl DT, Schubert JE, Jong-Levinger A, Sanders BF (2022) Grid edge classification method to enhance levee resolution in dual-grid flood inundation models. Adv Water Resour 168:104287

Kalcic MT, Underwood LW, Fletcher RM (2012) A new approach to monitoring coastal marshes for persistent flooding. In: AGU fall meeting abstracts vol. 2012, pp. OS41C-1753

Karamouz M, Fereshtehpour M (2019) Modeling DEM errors in coastal flood inundation and damages: a spatial nonstationary approach. Water Resour Res 55:6606–6624. https://doi.org/10.1029/2018WR024562

Kendall M (1975) Rank correlation measures. Charles Griffin, London

Krestenitis YN, Androulidakis YS, Kontos YN, Georgakopoulos G (2011) Coastal inundation in the north-eastern Mediterranean coastal zone due to storm surge events. J Coast Conserv 15(3):353–368

Krestenitis Y, Kombiadou K, Androulidakis Y, Makris C, Baltikas V, Skoulikaris C, Kontos Y, Kalantzi G (2015) Operational oceanographic platform in Thermaikos Gulf (Greece): forecasting and emergency alert system for public use. In: Proceedings of 36th international association of hydraulic research (IAHR) World Congress, The Hague, The Netherlands, 28 June–3 July 2015

Krestenitis Y, Pytharoulis I, Karacostas T, Androulidakis Y, Makris C, Kombiadou K, Tegoulias I, Baltikas V, Kotsopoulos S, Kartsios S (2017) Severe weather events and sea level variability over the Mediterranean Sea: the WaveForUs operational platform. In: Karacostas T, Bais A, Nastos PT (eds) Perspectives of atmospheric sciences Springer. https://doi.org/10.1007/978-3-319-35095-0_9

Lagouvardos K, Karagiannidis A, Dafis S, Kalimeris A, Kotroni V (2021) Ianos—a hurricane in the Mediterranean. Bull Am Meteorol Soc. https://doi.org/10.1175/BAMS-D-20-0274.1

Lionello P, Malanotte-Rizzoli P, Boscolo R, Alpert P, Artale V, Li L, Luterbacher J, May W, Trigo R, Tsimplis M, Ulbrich U (2006) The Mediterranean climate: an overview of the main characteristics and issues. Dev Earth Environ Sci 4:1–26

Lionello P, Conte D, Reale M (2019) The effect of cyclones crossing the Mediterranean region on sea level anomalies on the Mediterranean Sea coast. Nat Hazard 19(7):1541–1564

Makris C, Galiatsatou P, Tolika K, Anagnostopoulou C, Kombiadou K, Prinos P, Velikou K, Kapelonis Z, Tragou E, Androulidakis Y, Athanassoulis G, Vagenas C, Tegoulias I, Baltikas V, Krestenitis Y, Gerostathis T, Belibassakis K, Rusu E (2016) Climate change effects on the Marine characteristics of the Aegean and the Ionian Seas. Ocean Dyn 66(12):1603–1635. https://doi.org/10.1007/s10236-016-1008-1

Makris C, Androulidakis Y, Baltikas V, Kontos Y, Karambas T, Krestenitis Y (2019) HiReSS: storm surge simulation model for the operational forecasting of sea level elevation and currents in marine areas with Harbor works. In: Proceedings of 1st international scientific conference on design and management of port coastal and offshore works (DMPCO), 8–11 May 2019, vol 1. Athens, Greece, pp 11–15.

Makris C, Baltikas V, Androulidakis Y, Krestenitis Y (2020) Coastal inundation due to storm surges on a mediterranean deltaic area under the effects of climate change. In: Online proceedings of the 7th international conference on civil protection & new technologies, Safe Greece 2020. 14–16/10/2020, On-line. Part of ISSN 2654–1823

Makris C, Androulidakis Y, Karambas T, Papadimitriou A, Metallinos A, Kontos Y, Baltikas V, Chondros M, Krestenitis Y, Tsoukala V, Memos C (2021a) Integrated modelling of sea-state forecasts for safe navigation and operational management in ports: application in the Mediterranean Sea. Appl Math Model 89(2):1206–1234. https://doi.org/10.1016/j.apm.2020.08.015

Makris C, Baltikas V, Kontos Y, Androulidakis Y, Nagkoulis N, Kazakis I, Karambas T, Papadimitriou A, Metallinos A, Chondros M, Emmanouilidou M-E, Malliouri D, Klonaris G, Tsoukala V, Memos C, Spiliopoulos G, Zissis D (2021b) Integrated modelling of sea-state forecasts for safe navigation near and inside ports: the Accu-Waves platform. In: Proceedings of the 31st (2021b) international ocean and polar engineering conference, ISOPE, Rhodes, Greece, June 20–25, pp 2307–2314. ISSN 1098–6189

Makris CV, Tolika K, Baltikas VN, Velikou K, Krestenitis YN (2023) The impact of climate change on the storm surges of the Mediterranean Sea: coastal sea level responses to deep depression atmospheric systems. Ocean Model 181:102149. https://doi.org/10.1016/j.ocemod.2022.102149

Mann HB (1945) Nonparametric tests against trend. Econom J Econom Soc 245–259

Marcos M, Tsimplis MN, Shaw AG (2009) Sea level extremes in southern Europe. J Geophys Res Oceans, 114(C1)

Matsumoto K, Takanezawa T, Ooe M (2000) Ocean tide models developed by assimilating TOPEX/POSEIDON altimeter data into hydrodynamical model: a global model and a regional model around Japan. J Oceanogr 56(5):567–581

McFeeters SK (1996) The use of the normalized difference water index (NDWI) in the delineation of open water features. Int J Remote Sens 17(7):1425–1432

McFeeters SK (2013) Using the normalized difference water index (NDWI) within a geographic information system to detect swimming pools for mosquito abatement: a practical approach. Remote Sensing 5(7):3544–3561

Međugorac I, Orlic M, Janekovic I, Pasaric Z, Pasaric M (2018) Adriatic storm surges and related cross-basin sea-level slope. J Mar Syst 181:79–90

Miglietta MM, Moscatello A, Conte D, Mannarini G, Lacorata G, Rotunno R (2011) Numerical analysis of a Mediterranean 'hurricane'over south-eastern Italy: sensitivity experiments to sea surface temperature. Atmos Res 101(1–2):412–426

Miglietta MM, Laviola S, Malvaldi A, Conte D, Levizzani V, Price C (2013) Analysis of tropical-like cyclones over the Mediterranean Sea through a combined modelling and satellite approach. Geophys Res Lett 40:2400–2405

Murdukhayeva A, August P, Bradley M, LaBash C, Shaw N (2013) Assessment of inundation risk from sea level rise and storm surge in northeastern coastal national parks. J Coast Res 29(6A):1–16

Nastos PT, Papadimou KK, Matsangouras IT (2018) Mediterranean tropical-like cyclones: impacts and composite daily means and anomalies of synoptic patterns. Atmos Res 206:156–166

Neal J, Schumann G, Fewtrell T, Budimir M, Bates P, Mason D (2011) Evaluating a new LISFLOOD-FP formulation with data from the summer 2007 floods in Tewkesbury, UK. J Flood Risk Manag 4(2):88–95

Noyelle R, Ulbrich U, Becker N, Meredith EP (2019) Assessing the impact of sea surface temperatures on a simulated medicane using ensemble simulations. Nat Hazard 19(4):941–955

O'Neill AC, Erikson LH, Barnard PL, Limber PW, Vitousek S, Warrick JA, Foxgrover AC, Lovering J (2018) Projected 21st century coastal flooding in the Southern California Bight. Part 1: development of the third generation CoSMoS model. J Mar Sci Eng 6(2):59

Ogashawara I, Curtarelli MP, Ferreira, CM (2013) The use of optical remote sensing for mapping flooded areas. J Eng Res Appl 3:1956–1960.

Orlic M, Gacic M, Laviolette PE (1992) The currents and circulation of the Adriatic Sea. Oceanol Acta 15(2):109–124
Orlić M, Kuzmić M, Pasarić Z (1994) Response of the Adriatic Sea to the bora and sirocco forcing. Cont Shelf Res 14(1):91–116
Pandey S, Rao AD, Haldar R (2021) Modeling of coastal inundation in response to a tropical cyclone using a coupled hydraulic HEC-RAS and ADCIRC model. J Geophys Res Oceans 126(7):e2020JC016810
Pirazzoli PA, Tomasin A (2002) Recent evolution of surge-related events in the northern Adriatic area. J Coast Res pp 537–554
Pisano A, Marullo S, Artale V, Falcini F, Yang C, Leonelli FE, Santoleri R, Buongiorno Nardelli B (2020) New evidence of mediterranean climate change and variability from sea surface temperature observations. Remote Sens 12(1):132
Praskievicz S, Carter S, Dhondia J, Follum M (2020) Flood-inundation modeling in an operational context: sensitivity to topographic resolution and Manning's n. J Hydroinf 22(5):1338–1350
Pytharoulis I (2018) Analysis of a Mediterranean tropical-like cyclone and its sensitivity to the sea surface temperatures. Atmos Res 208:167–179
Pytharoulis I, Kartsios S, Tegoulias I, Feidas H, Miglietta MM, Matsangouras I, Karacostas T (2018) Sensitivity of a mediterranean tropical-like cyclone to physical parameterizations. Atmosphere 9(11):436
Pytharoulis I, Karacostas T, Tegoulias I, Kotsopoulos S, Bampzelis D (2015a) Predictability of intense weather events over northern Greece. 95th AMS Annual Meeting, 4–8 January, Amer. Meteor. Soc., Phoenix, Arizona, USA. Available online: https://ams.confex.com/ams/95Annual/webprogram/Paper261575.html. Accessed on 30 March 2022
Pytharoulis I, Tegoulias I, Kotsopoulos S, Bampzelis D, Karacostas T, Katragkou E (2015b) Verification of the operational high-resolution WRF forecasts produced by WAVEFORUS project. In: 16th Annual WRF Users' Workshop, 15–19 June, Boulder, Colorado, USA. https://www2.mmm.ucar.edu/wrf/users/workshops/WS2015b/extended_abstracts/p62.pdf. Accessed on 30 March 2022
Ramirez JA, Lichter M, Coulthard TJ, Skinner C (2016) Hyper-resolution mapping of regional storm surge and tide flooding: comparison of static and dynamic models. Nat Hazards 82(1):571–590
Sakamoto K, Tsujino H, Nakano H, Hirabara M, Yamanaka G (2013) A practical scheme to introduce explicit tidal forcing into an OGCM. Ocean Sci 9(6):1089–1108
Schmid K, Hadley B, Waters K (2014) Mapping and portraying inundation uncertainty of bathtub-type models. J Coast Res 30(3):548–561
Schwiderski EW (1980) On charting global ocean tides. Rev Geophys 18(1):243–268
Scicchitano G, Scardino G, Monaco C, Piscitelli A, Milella M, De Giosa F, Mastronuzzi G (2021) Comparing impact effects of common storms and Medicanes along the coast of south-eastern Sicily. Mar Geol 439:106556
Seenath A, Wilson M, Miller K (2016) Hydrodynamic versus GIS modelling for coastal flood vulnerability assessment: which is better for guiding coastal management? Ocean Coast Manag 120:99–109
Šepić J, Vilibić I, Lafon A, Macheboeuf L, Ivanović Z (2015) High-frequency sea level oscillations in the Mediterranean and their connection to synoptic patterns. Prog Oceanogr 137:284–298
Skamarock WC, Klemp JB, Dudhia J, Gill DO, Barker D, Duda MG, Huang XY, Wang W, Powers JG (2008) A description of the advanced research WRF version 3 (No. NCAR/TN-475+STR). University Corporation for Atmospheric Research. https://doi.org/10.5065/D68S4MVH
Skoulikaris C, Makris C, Katirtzidou M, Baltikas V, Krestenitis Y (2021) Assessing the vulnerability of a deltaic environment due to climate change impact on surface and coastal waters: the case of Nestos River (Greece). Environ Model Assess 26(4):459–486
Smith SD, Banke EG (1975) Variation of the sea surface drag coefficient with wind speed. Q J R Meteorol Soc 101(429):665–673
Tolika K, Makris Ch, Baltikas V, Velikou K, Krestenitis Y, (2021) On the assessment of RCMs in simulating deep cyclones over the Mediterranean region: impacts on the storm surges of coastal areas. In: Proceedings of the 15th international conference on meteorology, climatology and atmospheric physics (COMECAP), 26–29 September 2021, Ioannina, Greece
Toomey T, Amores A, Marcos M, Orfila A, Romero R, (2022) Coastal hazards of tropical—like cyclones over the Mediterranean Sea. J Geophys Res Oceans p e2021JC017964
Underwood LW, Kalcic MT, Fletcher RM (2012) Resolution enhancement of MODIS-derived water indices for studying persistent flooding. In: AGU fall meeting abstracts, vol. 2012, pp OS11D-1689
Vilibić I (2006) The role of the fundamental seiche in the Adriatic coastal floods. Cont Shelf Res 26(2):206–216
Vousdoukas MI, Voukouvalas E, Mentaschi L, Dottori F, Giardino A, Bouziotas D, Bianchi A, Salamon P, Feyen L (2016) Developments in large-scale coastal flood hazard mapping. Nat Hazard 16(8):1841–1853

Wahl T, Jain S, Bender J, Meyers SD, Luther ME (2015) Increasing risk of compound flooding from storm surge and rainfall for major US cities. Nat Clim Chang 5(12):1093–1097

Wang W, Bruyère C, Duda M, Dudhia, J, Gill D, Kavulich M, Keene K, Lin H-C, Michalakes J, Rizvi S, Zhang X, Beezley J, Coen J, Mandel J, Chuang H-Y, McKee N, Slovacek T, Wolff J (2014) ARW version 3 modeling system user's guide. NCAR-MMM pp. 413. https://www2.mmm.ucar.edu/wrf/users/docs/user_guide_V3/user_guide_V3.5/ARWUsersGuideV3.pdf. Accessed on 30 March 2022

West H, Horswell M, Quinn N (2018) Exploring the sensitivity of coastal inundation modeling to DEM vertical error. Int J Geogr Inf Sci 32(6):1172–1193

Williams LL, Lück-Vogel M (2020) Comparative assessment of the GIS based bathtub model and an enhanced bathtub model for coastal inundation. J Coast Conserv 24(2):1–15

Willmott CJ, Robeson SM, Matsuura K (2012) A refined index of model performance. Int J Climatol 32(13):2088–2094

Yin J, Yu D, Lin N, Wilby RL (2017) Evaluating the cascading impacts of sea level rise and coastal flooding on emergency response spatial accessibility in lower Manhattan, New York City. J Hydrol 555:648–658